

## On the dynamics of wave-mud interaction: A numerical study

Alec Torres-Freyermuth<sup>1,2</sup> and Tian-Jian Hsu<sup>1</sup>

Received 2 June 2009; revised 23 January 2010; accepted 12 March 2010; published 22 July 2010.

[1] Many previous studies consider wave attenuation over muddy seabeds and bottom boundary layer fluid-mud transport as two distinct research topics. Hence, various processes related to the physics of wave-mud interaction, such as turbulence-sediment interactions, rheological stresses, and nonlinear wave-wave interactions are incorporated rather artificially. The aim of this work is to present a new modeling approach which allows for the resolution of nonlinear wave propagation and bottom boundary layer mud transport with a single set of governing equations and closures. By adopting a fluid-mud modeling framework, a well-validated depth/phase-resolving wave propagation model, based on the Reynolds-Averaged Navier-Stokes (RANS) equations, is extended to model cohesive sediment transport. The numerical model consists of a set of governing equations based on the equilibrium Eulerian approach accurate for the fine sediment limit. The numerical model reduces to the clear fluid RANS equations when the sediment concentration approaches zero. Hence, the model is able to calculate continuously and consistently the nonlinear wave propagation, wave boundary layer processes, and fluid-mud transport without the need to prescribe the mud layer characteristics. Numerical simulations reveal several important physical processes that are critical for understanding the water-wave dynamics over muddy seabeds: (i) an enhancement of the wave boundary layer thickness due to the presence of the fluid-mud and rheological stress, which leads to a scaling relation between the enhanced wave boundary-layer and the fluid-mud layer and (ii) a direct wave amplitude dissipation due to rheological effects and clear evidences of low- and high-frequency wave attenuation via nonlinear energy transfer.

**Citation:** Torres-Freyermuth, A., and T.-J. Hsu (2010), On the dynamics of wave-mud interaction: A numerical study, *J. Geophys. Res.*, 115, C07014, doi:10.1029/2009JC005552.

### 1. Introduction

[2] The study of wave-mud interaction has drawn researchers' attention for over half a century because it entails many interesting physical processes of water wave mechanics and multiphase fluid dynamics that are not yet fully understood. Motivated by scientific/engineering applications, the study of wave-mud interaction has been branched into two main research efforts. As wave induced fluid-mud transport has been considered one of the key small-scale processes to determine the fate of terrestrial sediment in the coastal ocean [e.g., Harris *et al.*, 2005], many studies in this research area are focused on identifying the key mud-laden bottom boundary layer processes, such as turbulence-sediment interactions and effective settling velocity of flocculated

sediment [e.g., Vinzon and Mehta, 1998; Winterwerp, 2001]. On the other hand, studying wave attenuation over muddy seabeds is one of the classic wave hydrodynamic problems, beginning with the early work of Gade [1958] and with the eventual goal of developing large-scale wave propagation models for muddy seabeds [e.g., Kaihatu *et al.*, 2007; Winterwerp *et al.*, 2007; Rogers and Holland, 2009].

[3] Cohesive sediment transport can be classified into several modes primarily based on sediment concentration [Winterwerp and van Kesteren, 2004]. For instance, fluid-mud is a highly concentrated cohesive sediment suspension of mass concentration greater than about  $10 \text{ g l}^{-1}$  [Ross and Mehta, 1989]. Prior laboratory and small-scale modeling studies have identified several important mechanisms that control the dynamics of the fluid-mud transport, such as turbulence-sediment interactions, floc dynamics, rheological stresses and consolidation/swelling [Mehta, 1987; Dyer, 1989; Kranenburg, 1994; Toorman, 1999; Winterwerp, 1998, 2001]. Furthermore, a series of field observations [e.g., Ogston *et al.*, 2000; Traykovski *et al.*, 2000, 2007; Kineke *et al.*, 2006; Jaramillo *et al.*, 2009] have provided more insight into the realistic fluid-mud transport pro-

<sup>1</sup>Ocean Engineering Laboratory, Center for Applied Coastal Research, Department of Civil and Environmental Engineering, University of Delaware, Newark, Delaware, USA.

<sup>2</sup>Now at Laboratorio de Ingeniería y Procesos Costeros, Instituto de Ingeniería, Universidad Nacional Autónoma de México, Sisal, México.

cesses occurring in the wave boundary layer at the continental shelf.

[4] In contrast to nearshore hydrodynamics on sandy environments, there is a much stronger interplay between the near-bed sediment transport and the wave propagation characteristics in the presence of the fluid-mud. Early field observations [e.g., *Gade*, 1958; *Wells and Coleman*, 1981; *Forristall and Reece*, 1985] revealed large wave energy attenuation rates over muddy seabeds. As a result, several semi-analytical/numerical models [e.g., *Gade*, 1958; *Dalrymple and Liu*, 1978; *Yamamoto et al.*, 1995; *McPherson*, 1980; *Mei and Liu*, 1987; *Maa and Mehta*, 1990; *Foda et al.*, 1993; *De Wit*, 1995; *Kranenburg*, 2008; *Chan and Liu*, 2009] have been developed over the past few decades intended to contribute in our understanding of mud-induced wave transformation. Most of these modeling efforts simplified the problem as a two (or multi)-layer fluid system, where an inviscid water layer overlays a prescribed (thinner) mud layer with specific rheological properties (e.g., Newtonian, elastic, viscoelastic, viscoplastic) and characteristics (i.e., density, thickness, viscosity). This approach has been successfully applied to study the response of small/finite amplitude waves to prescribed mud layer properties. However, two-layer models often adopt a series of assumptions inherent in their derivation (e.g., small amplitude waves and homogenous fluid-mud characteristics) and hence dynamics of the water-mud system are coupled rather artificially.

[5] According to viscous (two-layer) models, the wave dissipation is larger when the Stokes wave boundary layer thickness is about the same order of magnitude of the mud layer thickness [e.g., *Gade*, 1958; *Dalrymple and Liu*, 1978; *Ng*, 2000], in agreement with the laboratory observations of *Gade* [1958]. These results have been incorporated in a nearshore spectral wave propagation model (SWAN) [*Booij et al.* 1999]) in order to simulate the mud-induced wave dissipation in muddy shelves [e.g., *Winterwerp et al.*, 2007; *Kranenburg*, 2008; *Rogers and Holland*, 2009]. For instance, *Winterwerp et al.* [2007] show a qualitative agreement between the numerical model and field observations from the Guyana muddy coast by employing representative values of fluid-mud in the numerical model. *Rogers and Holland* [2009] drive the wave propagation model employing in situ fluid-mud observations from Cassino Beach, Brazil. The wave predictions were compared against field observations finding a very good agreement only if smaller fluid-mud layer thickness than observed were considered. Nevertheless, the aforementioned models lack of a suitable parameterization for modeling nonlinear energy transfer in shallow waters.

[6] The importance of including nonlinear energy transfer in nearshore wave propagation models as an additional mechanism of wave energy attenuation in the presence of the fluid-mud has been recognized in recent investigations [e.g., *Sheremet and Stone*, 2003; *Elgar and Raubenheimer*, 2008]. Consequently, *Kaihatu et al.* [2007] incorporated the mud-induced dissipation model of *Ng* [2000] on a nonlinear wave propagation model in order to study the role of nonlinear wave interaction in the dissipation of short-waves in deep water. They hypothesized that the energy from high-frequencies is transferred to lower frequencies, which are able to interact directly with the bottom seabed, and hence the energy is lost in this manner [e.g., *Sheremet et al.*, 2005]. More recently, *Elgar and Raubenheimer* [2008] applied the

same hypothesis using an instrumentation array deployed in shallow water, where the triad-interactions approach resonance [*Elgar and Guza*, 1985]. In this latter investigation, a frequency-dependent dissipation rate function is derived based on field observations and (Boussinesq) model simulations. Contrary to the results obtained with viscous models [e.g., *Gade*, 1958; *Dalrymple and Liu*, 1978; *Ng*, 2000] and laboratory observations [e.g., *Gade*, 1958], they found that the peak wave damping rate occurs at the infragravity motions ( $f = 0.07$  Hz) which corresponds to a very small value of the ratio of the thickness of the mud layer to the Stokes wave boundary layer ( $d(\sigma/2\nu_m)^{1/2} \ll 1$ ). *Elgar and Raubenheimer* [2008] also indicate that the validity of the proposed frequency-dependent wave attenuation function is strongly dependent on the mud state, and hence its (generic) application in the field is not straightforward.

[7] Despite many mechanisms, such as turbulence closures, mud rheology, floc dynamics, and bottom erodibility, remain to be further investigated, mathematical/numerical modeling frameworks for fluid-mud transport have been developed in the past decade [e.g., *Winterwerp*, 2001; *Hsu et al.*, 2007, 2009] and have demonstrated to be effective in diagnosing or predicting wave-induced fluid-mud transport processes. In this study, a cohesive sediment transport modeling framework is implemented into a previously developed nonlinear wave propagation model (COBRAS [*Lin and Liu*, 1998]). Recently, *Hsu et al.* [2009] adopted this modeling framework, simplified for one-dimensional vertical boundary layer formulation, to study the dynamics of wave-supported gravity-driven mud flows. In the present work, the two-dimensional vertical formulation allows us the study of wave-mud interactions. The model is unique in that it allows the simulation of boundary layer processes, turbulence-sediment interaction, fluid-mud transport, and nonlinear free-surface wave transformation/dissipation, consistently and continuously with a single set of governing equations and closures without requiring to prescribe the matching conditions at the fluid-mud interface. We believe that this model provides a more complete and fully-coupled research tool that improves our current understanding on the mechanism of mud-induced wave attenuation. Unfortunately, detailed water column measurements on velocity, turbulence and sediment concentration profiles during wave-mud interaction are not available, which prevent us from carrying out detailed model validation. Hence, findings addressed in this paper are also inevitably of more qualitative nature.

[8] This paper is organized as follow. Section 2 is devoted to the model formulation, where the governing equations, boundary conditions, and closures are introduced. The numerical model is applied to study mud-laden boundary layer processes and wave dissipation/attenuation mechanisms in section 3. Finally, concluding remarks and future work are presented in section 4.

## 2. Model Description

[9] Due to flocculation and related chemical-biological effects [*Dyer*, 1989], modeling of cohesive sediment (mud) transport is more complex and empirically-based than that of noncohesive sediment (sand). However, several fundamental fluid dynamic mechanisms, such as turbulent sus-

pension, turbulence modulation due to the presence of sediment, and the rheological stress due to inter-particle (floc) interaction, remain similar. Therefore, it is possible to develop a numerical modeling framework for cohesive sediment transport using principles in multiphase fluid mechanics and turbulent flow modeling with additional parameterizations of the main cohesive sediment characteristics, such as floc dynamics and erodibility [e.g., *Winterwerp*, 2001; *Hsu et al.*, 2009].

[10] Cohesive sediments transport as flocs, which are loose aggregates composed of many primary particles, such as clay and silt. Therefore, one of the difficulties in modeling cohesive sediments is that the size and density of the floc aggregates may change due to the floc break-up and aggregation via small-scale turbulent shear and collisions [e.g., *Dyer*, 1989]. In reality, the dynamics of mud flocs is further complicated by chemical/biological processes that are difficult to quantify at micro-scale. For simplicity, the primary particles of cohesive sediments are not resolved in this study. Instead, we calculate floc aggregates with a prescribed constant floc diameter  $D$  and fractal dimension  $n_f$ , where the floc aggregate density  $\rho^a$  is obtained by assuming a fractal structure arrangement given by [*Kranenburg*, 1994]

$$\rho^a = \rho^f + \left(\frac{D}{D_0}\right)^{n_f-3} (\rho^s - \rho^f), \quad (1)$$

where  $\rho^f$  is the density of the fluid, and  $D_0$  and  $\rho^s$  are the diameter and density of the primary particle taken to be  $D_0 = 4 \mu\text{m}$  and  $\rho^s = 2650 \text{ Kg m}^{-3}$  in this study. The typical fractal dimension of suspended mud floc aggregate is around 2.0 [*Winterwerp*, 1998]. We specify a fixed floc size and hence the detailed floc break-up and aggregation processes are neglected here since floc dynamics is not the focus of the present study. Indeed, an estimation of flocculation timescale [e.g., *Winterwerp*, 1998] suggests that explicitly considering detailed floc break-up and aggregation processes may not change the qualitative characteristics of wave-induced fluid mud transport because the flocculation timescale (several minutes) is usually much larger than the typical timescale of waves considered in this study ( $T = 6 \text{ s}$ ). In summary, in the remaining of this paper we consider a fluid-particle system, driven by the passage of the waves, where the particle phase consists of many (spherical) floc particles with constant floc diameter  $D$  and density  $\rho^a$  (calculated by (1) via a prescribed constant fractal dimension).

## 2.1. Governing Equations

[11] The governing equations of the numerical model are obtained by simplifying the Eulerian two-phase flow equations for sediment-laden flow through the Equilibrium Eulerian approximation [*Ferry and Balachandar*, 2001] for fine sediment. The mathematical formulation for a fluid-particle system based on Eulerian two-phase flow equations [e.g., *Drew*, 1983] is the more general approach in that it is theoretically derived without strict limitation on particle diameter  $D$  or particle response time  $T_p$  (see (2) for its definition). However, in practical application, the inter-phase momentum transfer terms (e.g. drag) in the Eulerian two-phase formulation become infinitely large as particle

size approaches zero. Hence, a more robust approach is required for describing fine particles transport that are mathematically too fine to be efficiently calculated by the Eulerian two-phase formulation while at the same time remain to be too coarse/heavy to be described as completely passive substances [*Ferry and Balachandar*, 2001].

[12] The particle response time  $T_p$  is defined as

$$T_p = \frac{\rho^a D^2}{18\mu} f(\phi), \quad (2)$$

where  $\mu$  is the dynamic viscosity of the interstitial fluid, and  $f(\phi)$  is a function representing the hindered settling [*Richardson and Zaki*, 1954] which is dependent on the particle (floc) volume concentration  $\phi$ . The particle response time  $T_p$  represents the timescale required to accelerate a particle from rest to an equilibrium velocity driven by the ambient carrier flow. Typical mud floc in an energetic environment such as wave boundary layer has a floc diameter  $D$  of about  $O(10 \sim 100) \mu\text{m}$  and a floc density 30% to 70% greater than that of water (or seawater). The particle response time calculated by (2) for typical mud floc is smaller than  $O(10^{-3}) \text{ s}$ . Therefore, we can utilize the Equilibrium Eulerian approach in which the sediment velocities  $u_i^s$  are calculated by an expansion that depends on carrier fluid velocity field and particle response time [*Maxey*, 1987; *Ferry and Balachandar*, 2001]

$$u_i^s = u_i^f + T_p(1 - s^{-1})g_i - T_p \frac{Du_i^f}{Dt} + \frac{T_p}{\rho^a} \frac{\partial \tau_{ij}^s}{\partial x_j} + O(T_p^2), \quad (3)$$

with  $s = \rho^a/\rho^f$  the particle (floc) specific gravity,  $u_i^f$  and  $g_i = [0.0, 9.8] \text{ m s}^{-2}$  the  $i$ -th component of fluid velocity and gravitational acceleration, respectively. The second and third term in the right-hand-side (RHS) of (3) represent the sediment settling velocity  $W_s$  and the inertial effect due to fluid acceleration, respectively. The original derivation of the Equilibrium Eulerian approximation is based on analysis of a single particle and hence intergranular interaction is not considered [e.g., *Ferry and Balachandar*, 2001]. However, in a more concentrated flow there is a sufficient amount of particles contained within the averaging volume where the Eulerian formulation of sediment phase is derived. Hence, an additional term related to the intergranular stresses  $\tau_{ij}^s$  is incorporated in (3) in a more ad hoc sense to parameterize the enhanced mixing due to intergranular interaction. In the study of concentrated viscous suspensions of particles in viscous fluid [e.g., *Carpen and Brady*, 2002], the mixture formulation is often adopted. It can be shown that in order to derive the momentum equation similar to that of mixture formulation from the Eulerian two-phase formulation (see (6)), the intergranular interaction term shown in (3) needs to be incorporated. Therefore, we can argue that the mixture approach is consistent with the Fast Eulerian approximation for fine particles but with an addition of intergranular interactions.

[13] In the following derivation of the governing equations, we neglect the higher order terms in (3) and assume

$$u_i^s = u_i^f + T_p(1 - s^{-1})g_i + \frac{T_p}{\rho^a} \frac{\partial \tau_{ij}^s}{\partial x_j}. \quad (4)$$

Neglecting the flow acceleration term in (3) may be justified in the Reynolds-Averaged approach for the wave-driven sediment flow (outside the surf zone) where the flow acceleration is expected to be much smaller than the gravitational acceleration. On the other hand, intergranular interaction (rheological stress) is retained in this study because it is a major mechanism for hydrodynamic dissipation by muddy seabed.

[14] Hsu *et al.* [2003] presented the turbulence-averaged Eulerian two-phase flow equations for sediment transport in turbulent flow. This Eulerian two-phase formulation has been applied to study medium and coarse sediment transport in water under oscillatory flow [e.g., Amoudry *et al.*, 2008]. The governing equations for fine sediment used in this study are obtained by replacing the sediment velocities in the turbulence-averaged two-dimensional Eulerian two-phase equations of Hsu *et al.* [2003] by (4) based on the fast Eulerian approximation. The continuity equation of the present study is identical to the fluid-phase continuity equation of the Eulerian two-phase formulation

$$\frac{\partial(1-\phi)}{\partial t} + \frac{\partial(1-\phi)u_i^f}{\partial x_i} = 0, \quad (5)$$

where  $i = 1, 2$  in the present turbulence-averaged two-dimensional formulation. On the other hand, by replacing the sediment velocities  $u_i^s$  with (4) in the fluid momentum equation of the Eulerian two-phase formulation, we obtain a simplified flow momentum equation given by

$$\frac{\partial u_i^f}{\partial t} + u_j^f \frac{\partial u_i^f}{\partial x_j} = -\frac{1}{\rho^f} \frac{\partial p}{\partial x_i} + \frac{1}{\rho^f(1-\phi)} \left( \frac{\partial \tau_{ij}^f}{\partial x_j} + \frac{\partial \tau_{ji}^s}{\partial x_j} \right) + \frac{(s-1)\phi}{1-\phi} g_i, \quad (6)$$

where  $p$  is the fluid pressure. The flow momentum transport is caused by both fluid  $\tau_{ij}^f$  and sediment (rheological)  $\tau_{ji}^s$  stresses, being the latter only important when the sediment concentration is large. Notice that the gravitational term (last term in RHS of (6)) contains sediment concentration and therefore allows calculation of sediment-driven gravity flows [e.g., Hsu *et al.*, 2007, 2009].

[15] Substituting (4) into the continuity equation of the sediment phase [e.g., Hsu *et al.*, 2003], the governing equation for floc volume concentration  $\phi$  is derived

$$\frac{\partial \phi}{\partial t} + \frac{\partial \phi u_i^f}{\partial x_i} = \frac{\partial}{\partial x_i} \left[ \phi T_p (1-s^{-1}) g_i - \langle \phi'_i u'_i \rangle + \frac{\phi T_p}{\rho^a} \frac{\partial \tau_{ii}^s}{\partial x_i} \right], \quad (7)$$

where the first term on the RHS is the gravitational settling and the second term represents turbulent suspension (see equation (9)), whereas the third term is the gradient of sediment intergranular stress. The dominant component of sediment stresses in (7) is the vertical gradient of the sediment normal stresses, which serves as an additional mechanism for sediment suspension in concentrated regime. In most cohesive sediment transport studies, the intergranular normal stress is considered only in the concentrated aggregate network [Winterwerp and van Kesteren, 2004] where the mud bed consolidation and fluidization/liquefaction occur. In this study, we focus on studying fluid mud in mobile suspension above the aggregated network and hence

terms related to sediment stress in (7) are neglected and only sediment shear stress is considered in (6) due to its important role in wave energy dissipation.

[16] The commonly used fluid-mud mass concentration  $c$  ( $\text{g } \Gamma^{-1}$ ) is calculated from the computed floc volume concentration  $\phi$  as [Winterwerp and van Kesteren, 2004; Winterwerp *et al.*, 2006]

$$c = \rho^s \phi \left( \frac{D}{D_0} \right)^{\eta_f - 3} = \rho^s \phi \left( \frac{\rho^a - \rho^f}{\rho^s - \rho^f} \right). \quad (8)$$

## 2.2. Closures

[17] The numerical solution of (6) and (7) requires closures on turbulent Reynolds stresses, turbulent suspension, and sediment rheological stresses and appropriate boundary conditions for flow velocities, pressure, and sediment concentration.

### 2.2.1. Turbulent Suspensions

[18] Eddy viscosity assumption is adopted in this study to parameterize Reynolds stresses (see section 2.2.2). Hence, in analogy with the turbulent momentum transport, we calculate the turbulent suspension of sediment via the gradient transport assumption

$$\langle \phi'_i u'_i \rangle = -\frac{\nu_t}{\sigma_c} \frac{\partial \phi}{\partial x_i}, \quad (9)$$

with  $\sigma_c$  being the Schmidt number often specified empirically. In this study we adopt the value of 0.5, which is found to be the optimal value using the one-dimensional vertical version of the current model [Hsu *et al.*, 2007] for modeling (noncohesive) sediment transport in a steady flow. Numerical experiments suggest that the present model results remain qualitatively similar when  $\sigma_c$  is increased or decreased by 50%.

### 2.2.2. Reynolds Stressess

[19] The Reynolds stresses are calculated by the eddy viscosity assumption employing a two-equation  $k - \epsilon$  turbulence closure model. A more sophisticated turbulence closure scheme may be adopted. However, the choose of the eddy viscosity assumption and a two-equation closure responds to the need of providing a formulation for capturing essential physics of near-bed fluid mud transport while at the same time allows computing nonlinear wave propagation over (for) long distance (duration) in an affordable computational time. Based on the eddy viscosity assumption the total fluid stress, including the fluid viscous stress, is calculated as

$$\begin{aligned} \tau_{ij}^f &= \rho^f (\nu + \nu_t) \left( \frac{\partial u_i^f}{\partial x_j} + \frac{\partial u_j^f}{\partial x_i} \right) - \frac{2}{3} \rho^f (\nu + \nu_t) (1-\phi) k \delta_{ij} \\ &\quad - \frac{2}{3} \rho^f \nu_t \frac{\partial u_k}{\partial x_k} \delta_{ij}, \end{aligned} \quad (10)$$

where  $\delta_{ij}$  is the Kronecker delta,  $\nu$  is the kinematic viscosity, and the turbulent eddy viscosity  $\nu_t$  is related to the fluid turbulence kinetic energy  $k$  and turbulent dissipation rate  $\epsilon$  by

$$\nu_t = C_\mu \frac{k^2(1-\phi)}{\epsilon}. \quad (11)$$

[20] The balance equation for turbulent kinetic energy in particle-laden turbulence flow can be derived from the Eulerian two-phase mass and momentum equations [Elghobashi and Abou-Arab, 1983]. Following the earlier study of wave-induced fluid mud transport [Hsu *et al.*, 2007], the balance equations for  $k$  and  $\epsilon$  are given by

$$\begin{aligned} \frac{\partial(1-\phi)k}{\partial t} + \frac{\partial(1-\phi)ku_j^f}{\partial x_j} &= \frac{\tau_{ij}^f}{\rho^f} \frac{\partial u_i^f}{\partial x_j} + \frac{\partial}{\partial x_j} \left[ \left( \nu + \frac{\nu_t}{\sigma_k} \right) \frac{\partial(1-\phi)k}{\partial x_j} \right] \\ &\quad - (1-\phi)\epsilon - \frac{2\phi sk}{T_p + T_L} - (s-1)g_z \frac{\nu_t}{\sigma_\epsilon} \frac{\partial \phi}{\partial z} \end{aligned} \quad (12)$$

and

$$\begin{aligned} \frac{\partial(1-\phi)\epsilon}{\partial t} + \frac{\partial(1-\phi)\epsilon u_j^f}{\partial x_j} &= C_{\epsilon 1} \frac{\epsilon}{k} \frac{\tau_{ij}^f}{\rho^f} \frac{\partial u_i^f}{\partial x_j} + \frac{\partial}{\partial x_j} \left[ \left( \nu + \frac{\nu_t}{\sigma_k} \right) \frac{\partial(1-\phi)\epsilon}{\partial x_j} \right] \\ &\quad - C_{\epsilon 2} \frac{\epsilon^2}{k} (1-\phi) - C_{\epsilon 3} \frac{\epsilon}{k} \left[ \frac{2\phi sk}{T_p + T_L} \right] \\ &\quad - C_{\epsilon 4} \frac{\epsilon}{k} \left[ (s-1)g_z \frac{\nu_t}{\sigma_\epsilon} \frac{\partial \phi}{\partial z} \right]. \end{aligned} \quad (13)$$

As compared to the standard  $k$ -equation for clear fluid, the  $k$ -equation derived from the two-phase formulation has additional dissipation (or production) terms for carrier flow turbulence due to sediment. As shown in (12) and (13), there are two major dissipation mechanisms for carrier flow turbulence due to the presence of sediment. The first dissipation mechanism (the second to the last term in (12) and (13)) is to parameterize the slip fluctuating velocities between the fluid and the sediment phases originated from viscous drag in the Eulerian two-phase momentum balance with the fluid eddy turn-over time calculated as  $T_L = 0.165 k/\epsilon$ . The second dissipation mechanism is due to stable density stratification caused by the presence of sediment (the last term in (12) and (13)). It is noted that in the present formulation for fine sediment it is assumed that ensemble-averaged sediment velocities closely follow the fluid velocity through (4). However, this may not suggest that sediment and fluid velocity fluctuations closely follow each other in turbulent flow. Specifically for high frequency velocity fluctuations, the timescale of these smaller eddies may be comparable to that of the particle response time. Hence, we argue here that even for fine cohesive sediment (flocs), both the sediment density stratification and the difference of fluctuating velocities between the fluid and sediment phase can cause damping of carrier flow turbulence and control the existence of wave-induced fluid mud transport [Hsu *et al.*, 2009].

[21] Standard  $k - \epsilon$  model coefficients ( $C_{1\epsilon} = 1.44$ ,  $C_{2\epsilon} = 1.92$ ,  $\sigma_k = 1.0$ , and  $\sigma_\epsilon = 1.3$ ) are utilized in this study [e.g., Rodi, 1993]. The model coefficient  $C_{3\epsilon}$  associated with the damping term due to viscous drag in the  $\epsilon$  equation is set to be  $C_{3\epsilon} = 1.2$  following earlier work for dilute particle-laden flow [Elghobashi and Abou-Arab, 1983; Hsu *et al.*, 2003]. On the other hand, there are many suggested choices in the literature of stratified flow [e.g., Rodi, 1987; Umlauf and Burchard, 2005] for the empirical coefficient  $C_{4\epsilon}$  associated with the density stratification term in the  $\epsilon$ -equation. Following Rodi [1987] we set  $C_{4\epsilon} = 0$  for stable density stratification. Examining the model results for wave-induced fluid mud transport (see section 3.1), we find that

the viscous drag is the more important damping term of carrier flow turbulence due to high sediment concentration near the bed, while the density stratification term is small very close to the bed because it scales with the eddy viscosity (and hence the distance from the bed). Therefore, model results presented here are not very sensitive to the model coefficient  $C_{4\epsilon}$ . However, model results on suspended sediment concentration are more sensitive to the value of  $C_{3\epsilon}$ . Setting  $C_{3\epsilon} = 1.2$  appears to give reasonable fluid mud concentration when compared with the limited field observations [Hsu *et al.*, 2007, 2009].

### 2.2.3. Sediment Stresses

[22] The rheological behavior of fluid-mud is quite complex because of its dependence on sediment concentration, grain properties, stage of consolidation, floc structure, and biological/chemical processes. The rheological stress affects the flow directly through the momentum equation and hence dictates the hydrodynamic dissipation of the propagating waves. Unlike noncohesive (also relative massive) particles where the closure of intergranular stresses is more well-understood [e.g., Campbell, 1990], closure of sediment stresses for flocculated particles is more complicated due to the evolution of floc structure [e.g., Toorman, 1997], irregular shape of the floc aggregates, and interstitial fluid effects [e.g., Carpen and Brady, 2002]. However, there is a general consensus that the rheological stress of the concentrated floc aggregate may behave as highly viscous fluid and fluid-solid like behavior i.e. yield stress characteristic for low shear rate and high concentration conditions [e.g., Mei and Liu, 1987; Frigaard and Nouar, 2005].

[23] In this study, the sediment rheological stresses are calculated based on a simple mathematical formulation given by Le Hir *et al.* [2001], where the sediment shear stresses are calculated as

$$\tau_{ij}^s = \tau_{ji}^s = \rho^f \nu_s \sigma_{ij} \quad (14)$$

and the sediment effective viscosity  $\nu_s$  in (14) is given by

$$\nu_s = \nu_{s0} \phi^{k_a} \left[ 1 + \frac{\gamma_0}{k_b \gamma_0 + |\sigma_{ij}|} \right]. \quad (15)$$

The sediment effective viscosity is empirically parameterized as a nonlinear function of concentration  $\phi$  and the strain-rate of the mean flow  $\sigma_{ij} = (\partial u_i^f / \partial x_j + \partial u_j^f / \partial x_i)$ , which increases with mud concentration via a power law function with a prescribed coefficient  $k_a$ . Therefore, the wave dissipation is highly dependent on the value of this coefficient. The reference value of the sediment effective viscosity is specified by  $\nu_{s0}$ . The parameter  $k_b$  controls the yield stress (stiffness) of the water-mud mixture. It is noted that  $\gamma_0$  is set to be  $1.0 \text{ s}^{-1}$  in order to make the coefficient  $k_b$  dimensionless and hence  $\gamma_0$  is not an empirical coefficient. Given sufficient rheological information, these coefficients can be obtained by the best-fit of (15) to the measured data. For fluid mud transport, these empirical coefficients are usually unknown and hence the purpose of this study is not to predict wave energy dissipation for a specific experiment or field observation but to utilize the numerical model as a tool to diagnose the dynamics of wave-mud interactions. Although this is a non-Newtonian closure, notice that the  $k_b$

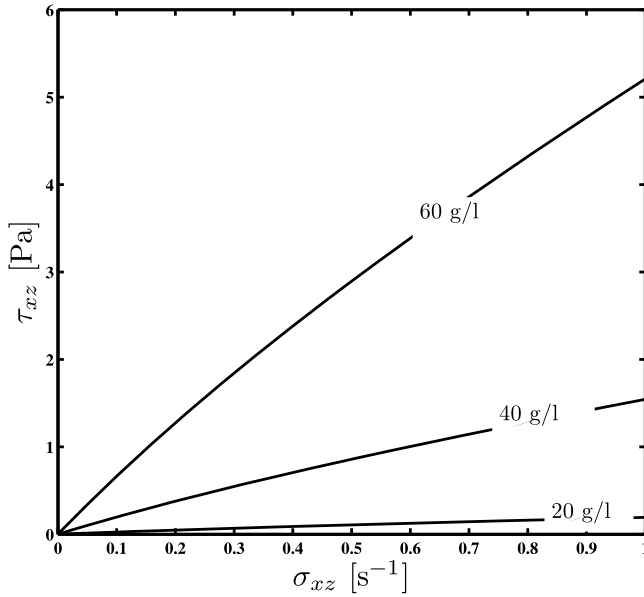


**Figure 1.** Stress-strain relation based on (14)–(16) for three different sediment mass concentrations.

coefficient controls the viscosity dependence on strain-rate values and hence Newtonian-like rheology behavior can be simulated by setting  $k_b = 1.0$  (see Figure 1). Here, the numerical coefficients for rheology are specified as follows:

$$\nu_{s0} = 0.005(\text{m}^2\text{s}^{-1}), \quad k_a = 3.0, \quad k_b = 1.0. \quad (16)$$

As shown in Table 3, these coefficients gives bulk mud effective viscosity of  $O(10^{-3}) \text{ m}^2 \text{ s}^{-1}$ , which is consistent with limited observed data for fluid mud [e.g., *Mei and Liu, 1987*]. In this study, we focus on fluid mud mass concentration ranging from about  $10 \sim 60 \text{ g l}^{-1}$ . Based on the maximum suspended sediment concentration investigated in this study, mud transport modeled here can be also referred to high-concentrated mud suspension [*Winterwerp and van Kesteren, 2004*]. At these concentrations, it is expected that the fluid mud does not have a yield or pseudo-plastic (shear thinning) behavior and hence assuming a Newtonian rheology is appropriate. It is worth to mention that the maximum fluid-mud concentration considered in this investigation is smaller than previously published studies. It is noted again that only the fluid mud transport above the aggregate network is considered here and hence closures of normal stresses are not incorporated at this point.

### 2.3. Numerical Implementation and Boundary Conditions

[24] The governing equations and closures for the wave-mud interaction model are solved numerically by extending an existing nonlinear wave propagation model (COBRAS [*Lin and Liu, 1998*]) which solves the two-dimensional vertical Reynolds-Averaged Navier-Stokes (RANS) equations with a volume of fluid (VOF) scheme for free-surface tracking. The original COBRAS code and its extended versions have been widely validated for the study of various water wave problems. However, the numerical model

applications have not been extended to study wave-mud interaction.

[25] Finite difference scheme with staggered grid system is utilized in the numerical model [*Lin and Liu, 1998*]. The advection-diffusion equation of sediment concentration is solved in the beginning of each computational cycle with combined upwind and central difference method. The flow mass and momentum equations are then solved by revising the two-step projection method for the present continuity equation that involves sediment concentration [*Hsu and Liu, 2004*]. The  $k - \epsilon$  equations are then calculated to obtain turbulence information and the location of the flow free-surface is updated by the VOF scheme at the end of the computational cycle. The time step for each computational cycle is determined based on the Courant number  $C_r$  criterion for the convection terms ( $C_r = 0.3$ ) and CFL criterion for diffusion terms controlled by the maximum value of turbulent eddy viscosity and sediment effective viscosity. For the fluid mud simulations, the minimum time step is usually constrained by sediment effective viscosity which is of  $O(10^{-5})\text{s}$ . More detailed description of the numerical implementation are given by *Lin and Liu* [1998].

#### 2.3.1. Near-Bed Boundary Condition

[26] In order to model wave propagation over a sufficient distance such that a significant amount of wave energy dissipation can be detected, the minimum vertical grid size  $\Delta z$  that is used to resolve the near bed wave boundary layer and fluid mud transport is of few millimeters. Such a grid resolution is sufficient to resolve the overall wave boundary layer flow structure with appropriate near-wall modeling. However, it remains too coarse to resolve the viscous sub-layer and buffer layer using a typical low-Reynolds number two-equation closure. From the fluid mud transport perspective, the bottom boundary of the present model is located at the interface between the concentrated aggregate network and the mobile fluid mud. Hence, the present model calculates the fluid mud transport above the concentrated aggregate network with floc concentration smaller than gelling concentration [*Winterwerp and van Kesteren, 2004*].

[27] Due to the presence of fluid and sediment stresses in the momentum equation, the bottom boundary condition for horizontal velocity  $u$  shall include both the fluid component  $\tau_b^f$  and sediment component  $\tau_b^s$ . At present, there is no general near-wall modeling for flow velocity profile that is appropriate for both dilute and concentrated conditions. Due to the lack of information, the sediment bottom stress  $\tau_b^s$  is estimated directly using (14) and (15) by assuming a no-slip boundary condition for flow velocity. Hence, it is assumed that when fluid mud concentration is large, the flow velocity very near the bed can be extrapolated with a linear profile from the horizontal velocity  $u$  calculated at half grid point  $\Delta z/2$  above the bed. On the other hand, the fluid bottom stress is calculated by a (fluid) friction velocity  $u_*$ , i.e.  $\tau_b^f = \rho u_*^2$ , where the (fluid) friction velocity is further calculated by assuming that a logarithmic velocity profile is valid between the bottom and the half grid point above the bed

$$u_* = \frac{\kappa u(\Delta z/2)}{\ln \left[ \frac{30\Delta z/2}{K_s} \right]}, \quad (17)$$

where  $\kappa = 0.4$  is the von Karman constant and the roughness  $K_s$  is set to be five floc diameters in most of the model

**Table 1.** Simulated Cases

Case	$H$ (m)	Fluid-Mud	Roughness, $K_s$ (m)	Erodibility, $\beta$ (m s <sup>-1</sup> )	Rheology, $\nu_{s0}$ (m <sup>2</sup> s <sup>-1</sup> )
<i>Progressive Monochromatic Waves</i>					
1A	0.74	Yes	$1.1 \times 10^{-4}$	$1.0 \times 10^{-2}$	$5.0 \times 10^{-3}$
1B	0.74	No	$1.1 \times 10^{-4}$	-	-
1C	0.74	Yes	$1.1 \times 10^{-4}$	$1.0 \times 10^{-2}$	$5.0 \times 10^{-4}$
1D	0.40	Yes	$1.1 \times 10^{-4}$	$1.0 \times 10^{-2}$	$5.0 \times 10^{-3}$
1E	0.88	Yes	$1.1 \times 10^{-4}$	$1.0 \times 10^{-2}$	$5.0 \times 10^{-3}$
1F	0.74	No	$1.0 \times 10^{-1}$	-	-
1G	0.74	Yes	$1.1 \times 10^{-4}$	$1.0 \times 10^{-4}$	$5.0 \times 10^{-3}$
1H	0.74	Yes	$1.1 \times 10^{-4}$	$1.0 \times 10^{-5}$	$5.0 \times 10^{-3}$
<i>Wave Groups</i>					
2A	0.5	Yes	$1.1 \times 10^{-4}$	$1.0 \times 10^{-2}$	$5.0 \times 10^{-3}$
2B	0.5	No	$1.1 \times 10^{-4}$	-	-
2C	0.5	No	$6.0 \times 10^{-2}$	-	-
2D	0.5	No	$1.0 \times 10^{-1}$	-	-

simulations to represent typical flat bed (small roughness) condition (i.e., 0.11 mm, see Table 1). Even for dilute mud-laden wave boundary layer, turbulence modulation due to the presence of sediment can affect the velocity profile near the bed and hence  $K_s$  and  $\kappa$  in the near-wall modeling shall depend on flow condition and sediment concentration [e.g., Hsu *et al.*, 2003; Toorman, 2008; Cantero *et al.*, 2009]. However, these more complicated logarithmic formulations are not pursued in this investigation. In fact, one can also argue that the extrapolation functions used for estimating  $\tau_b^s$  (linear) and  $\tau_b^f$  (logarithmic) are also seemingly inconsistent. We must note here that for most of the model results discussed in the next section, the suspended mud concentration is large enough such that the near bed shear stress is completely dominated by sediment stress and hence the uncertainties in estimating  $\tau_b^f$  using (17) become negligible. On the other hand, (17) remains to be calculated in the numerical model to estimate  $\tau_b^f$  in order to develop a more general numerical model that can also be used to calculate the turbulent boundary layer without mud or with dilute sediment transport (see Table 1 where clear fluid flow cases are also calculated as control numerical experiments).

[28] In a clear flow turbulent boundary layer, the bottom boundary condition for the turbulent kinetic energy  $k$  is often specified using the bottom friction velocity [e.g., Rodi, 1993]. For sediment-laden boundary layer, sediment concentration affects the flow turbulence and is modeled by the additional dissipation terms in the  $k - \epsilon$  equations. To incorporate a bottom boundary condition for  $k$  that is more consistent with the present sediment-laden flow, we chose a no-flux boundary condition for  $k$ , as suggested by earlier studies [e.g., Hagatun and Eidsvik, 1986]

$$\frac{\partial k}{\partial z} = 0 \quad (18)$$

and the boundary condition for the turbulence dissipation rate  $\epsilon$  is calculated with a standard near-wall approximation

$$\epsilon = \frac{C_\mu^{3/4} k^{3/2}}{\kappa z}. \quad (19)$$

[29] A flux boundary condition is adopted to specify the amount of upward sediment flux suspended from the bottom into the mobile fluid mud regime. This upward erosion flux

$E$  (m s<sup>-1</sup>) is estimated by the following parameterization [e.g., Partheniades, 1965; Sanford and Maa, 2001; Hsu *et al.*, 2009]:

$$E = \beta \left( \frac{\tau_b^f(t)}{\tau_c} - 1 \right), \quad (20)$$

where both the empirical parameter  $\beta$  and the critical shear stress  $\tau_c$  control the magnitude of  $E$  for a given fluid bottom stress  $\tau_b^f$ , and hence they are often called erodibility parameters. Unlike noncohesive sediment, these erodibility parameters for cohesive sediment are not only a function of primary grain properties but also depend on the stage of consolidation, floc structure, and chemical-biological effects. Hence, the erodibility parameters for cohesive sediment are often empirically determined via in-situ erodibility tests [e.g., Sanford and Maa, 2001]. In general, quantitative predictions on bottom mud suspension is not possible unless these empirical parameters are determined in-situ. Due to the uncertainties in erodibility parameters (and rheological parameters mentioned previously) of the mud layer, the primary goal of this study is not to accurately predict the amount of mud suspension driven by a given wave condition. On the contrary, this study focuses on studying the dissipation and nonlinear energy transfer mechanisms of water waves due to bottom mud suspension driven by a given set of rheology and erodibility parameters.

### 2.3.2. Wave Boundary Conditions

[30] In the numerical model, the wave is generated by specifying both the velocity profile and the free-surface elevation time series at the inflow (left) boundary [Lin and Liu, 1998]. The forcing boundary can also consider corrections for active wave absorption in case that significant reflected wave energy reaches the inflow boundary. Also, when the wave group (irregular wave) generation is sought, for a more realistic wave forcing, the second-order bound-wave is incorporated via Longuet-Higgins and Stewart [1960].

## 3. Model Results

[31] The numerical model is employed to study wave-mud interaction under different scenarios (see Table 1). Monochromatic progressive wave and wave groups are considered in order to investigate different aspects of mud-

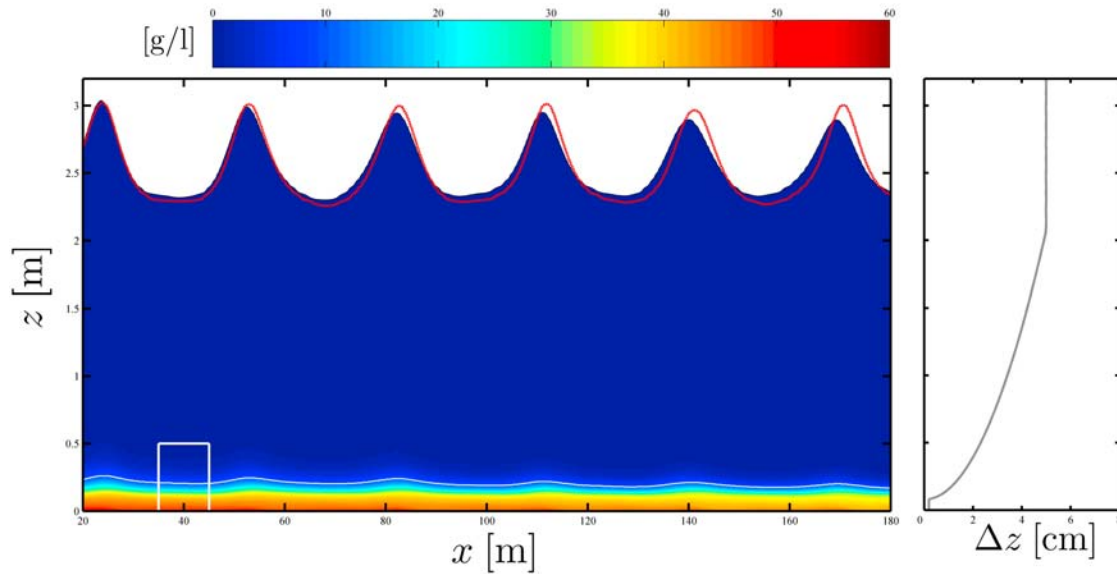


**Figure 2.** (left) Snapshot of the model results for free surface elevation and mud concentration beneath a progressive wave. The dashed curve depicts the free-surface elevation in an independent simulation without the fluid-mud and the solid white curve depicts the lutocline location given by the  $10 \text{ g l}^{-1}$  concentration threshold. (right) The vertical (nonuniform) grid resolution is shown.

laden wave boundary layer process and nonlinear wave interactions. In order to contrast the effect of fluid mud, a reference case for clear fluid flow (without sediment) is computed for the two different wave types (see third column of Table 1). In addition, to test the feasibility of parameterizing the effect of fluid-mud on hydrodynamic dissipation via drastically enhanced bed roughness, large seabed roughness heights  $K_s$  are specified in the clear fluid simulation for several selected cases (fourth column of Table 1). For the cases with fluid-mud transport, the erodibility parameters ( $\tau_c$  and  $\beta$ ) control the amount of fine sediment in suspension and thus the resulting fluid-mud concentration. In this study, several erodibility conditions are tested via adjusting  $\beta$  (fifth column of Table 1). The mud rheology coefficients remain the same in all simulated cases (with fluid-mud) except in case 1C where the reference viscosity  $\nu_{s0}$  is decreased. In all computed tests with cohesive sediment, a floc size of  $22 \mu\text{m}$  and specific gravity of  $s = 1.34$  are specified, which gives a fractal dimension of  $n_f = 2.08$  (see (1)). In most of the simulated tests the maximum volumetric concentration is around 12% ( $50 \text{ g/l}$ ).

[32] The objective of employing monochromatic progressive waves is twofold. First, this simple wave type is used to illustrate the fluid-mud dynamics and its scaling relation with the wave boundary layer (section 3.1). Secondly, monochromatic waves allow a straightforward model verification against two-layer theory, and the further study of wave attenuation (section 3.2).

[33] A cnoidal wave train propagating in a constant water depth of  $h = 2.5 \text{ m}$  is sent into the numerical wave flume (Figure 2). A nonuniform fine grid ( $\min(\Delta z) = 2 \text{ mm}$ ) in the vertical direction (Figure 2 (right)) allows the resolution of the wave boundary layer flow structure near the bed, while a uniform grid ( $\Delta x = 25 \text{ cm}$ ) in the cross-shore direction is chosen to resolve the surface wave propagation. A snapshot of the model results (Figure 2) for case 1A, after calculating

thirty propagating waves (model results reach quasi-stationary state), illustrates the free-surface elevation (solid curve) and sediment suspension beneath the wave. Fine sediments are suspended and remain concentrated within about 10–20 cm from the seabed with mass concentration around 10 to  $60 \text{ g l}^{-1}$ , exceeding the criterion of fluid-mud. In addition, the free-surface elevation for the corresponding clear fluid simulation is also plotted (case 1B, dashed curve). Differences in wave amplitude and phase between the two test cases are caused by the effect of fluid-mud on damping the wave energy and modifying the wave length as waves propagate downstream of the flume. The lutocline is also shown in Figure 2 (solid curve at around 20 cm above the bed), which can be considered as an indicator for fluid mud layer thickness. Figure 2 further suggest that the fluid-mud layer thickness slightly decreases downstream and that there is a phase lead between the lutocline wave and the surface wave. Both features being the result of the coupling of the wave-mud system. An important characteristic of this model is that the calculated fluid-mud layer is inhomogeneous in the vertical direction, without the unrealistic sharp interface between the clear fluid and the mud layer which is a major assumption in two-layer models.

### 3.1. Fluid-Mud Dynamics

[34] The effect of sediment on the fluid flow is more important near the bed where the sediment concentration and sediment rheological stresses become large. Thus, the wave boundary layer structure is expected to be modified with the presence of concentrated fluid-mud. At present, it remains difficult to measure high resolution time-dependent velocity profiles through the fluid-mud layer in the field [Traykovski *et al.*, 2000; Jaramillo *et al.*, 2009]. For this reason, we rely on the numerical model to provide new insights into the processes occurring in this highly concentrated region. The observed wave boundary layer thickness



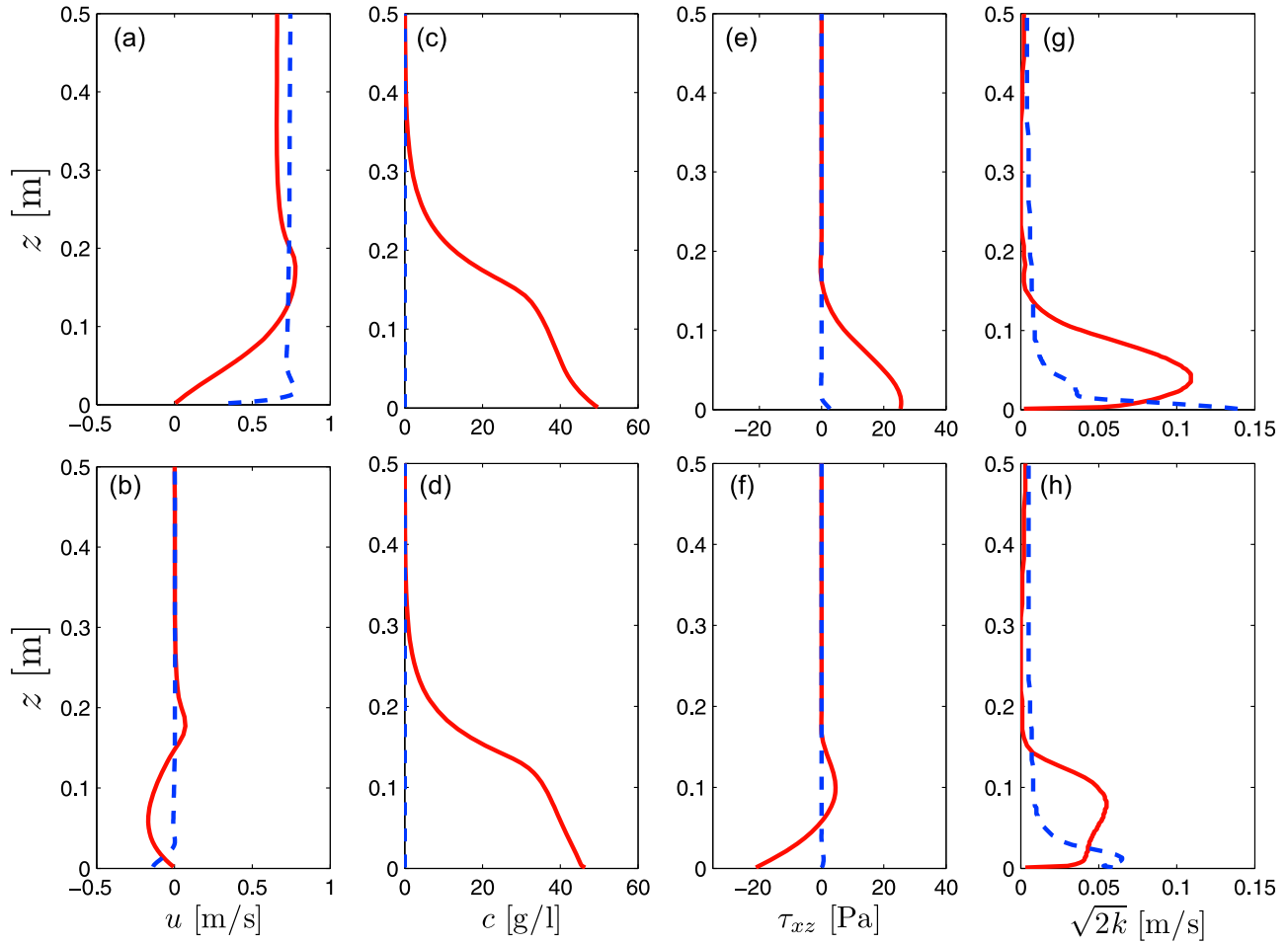


**Figure 3.** Instantaneous vertical profiles at the instant of (top) maximum free-stream and (bottom) at flow reversal for the (a and b) horizontal velocity, (c and d) sediment concentration, (e and f) total shear stresses, and (g and h) turbulent intensity in cases 1A (solid curve) and 1B (dashed curve).

in the numerical model  $\delta_{obs}$  is defined as the distance between the bed and the maximum near bottom velocity at the maximum free-stream velocity phase, i.e.  $\omega t = 90^\circ$  [see *Jensen et al.*, 1989, Figure 24]. Also, the following two widely-used definitions of the lutocline location (fluid-mud thickness) are adopted in this work: (I) the vertical distance between the  $10 \text{ g l}^{-1}$  concentration contour and the bottom [Ross and Mehta, 1989; Traykovski et al., 2000] and (II) the distance from the bottom to the position of the maximum vertical concentration gradient [Lamb et al., 2004; Cantero et al., 2009].

[35] Figure 3 shows the profiles of the time-dependent horizontal velocity  $u$  (Figures 3a and 3b), mass concentration  $c$  (Figures 3c and 3d), total shear stresses (Figures 3e and 3f), and turbulent intensity  $\sqrt{2k}$  (Figures 3g and 3h) at the phase of maximum free-stream velocity (Figure 3 (top)) and flow reversal (Figure 3 (bottom)), for cases 1A (solid curve, with fluid mud) and 1B (dashed curve, clear fluid). The profiles shown in Figure 3 correspond to the downstream location  $x = 40 \text{ m}$  depicted by the rectangle in Figure 2. The velocity profiles when fluid mud is present (Figures 3a and 3b, solid curve) show a significant increase, of up to four times, in the wave boundary layer thickness with respect to the clear fluid condition (dashed curve). In

this case, the enhanced wave boundary layer is about the same thickness of the fluid-mud layer defined according to definition (II) (see case 1A in Table 2). The numerical model predicts the commonly observed phase shift (i.e. overshoot) of the flow velocity in the wave boundary layer with respect to the free-stream velocity [Trowbridge and Madsen, 1984; Jensen et al., 1989]. Figures 3c and 3d illustrate the mass concentration profiles at the phase of maximum free-stream velocity and flow reversal. Due to the low settling velocity of fine sediments ( $O(10^{-1}) \text{ mm s}^{-1}$ ), the concentration profiles are similar at different wave phases once a quasi-stationary condition is reached in the numerical flume. However, there is a noticeable vertical variation in sediment concentration at the upper portion of the profile ( $z > 0.12 \text{ m}$ ), which is related to the small lutocline wave developed near the water-mud interface where the sediment concentration gradient is larger.

[36] In Figures 3e and 3f the total shear stresses, including the fluid turbulent stress, fluid viscous stress (negligibly small), and sediment rheological stress, are shown. The total shear stresses are significantly larger when fluid mud is present due to the additional contribution from the sediment rheological stresses. Without fluid mud, the major contribution to the total stress is the turbulent stress (dashed

**Table 2.** Wave Boundary Layer and Fluid-Mud Thickness

Case	$\delta_{obs}$ (m)	$\delta_1$ (m)	$d$ (m)	$d/\delta_{obs}$	$d/\delta_1$
1A	0.165	0.150	0.145	0.873	1.038
1C	0.073	0.088	0.070	0.959	1.253
1D	0.112	0.091	0.100	0.893	0.914
1E	0.190	0.170	0.170	0.895	1.000
1G	0.160	0.135	0.170	1.063	0.793
1H	0.110	0.110	0.140	1.273	0.791

curve) and its magnitude is much smaller. According to (14) and (15), the magnitude of the sediment viscosity and rheological stress are related to sediment concentration, being larger closer to the bed. The large sediment viscosity ( $\nu_m = O(10^{-4}) - O(10^{-2}) \text{ m}^2 \text{ s}^{-1}$ ) makes the vertical mixing of flow momentum much more effective and increases the thickness of the wave boundary layer. The enhanced viscosity and boundary layer thickness can also induce more hydrodynamic energy dissipation. Hence, when the wave boundary layer is laden with concentrated fluid mud, the sediment rheological stress becomes the critical mechanism for the vertical mixing of flow momentum and dissipation of wave energy.

[37] The enhanced wave boundary layer thickness due to sediment rheological stress also affects the turbulence characteristics inside the wave boundary layer (see Figures 3g and 3h). For the clear fluid condition, the maximum turbulent intensity is observed near the bed (dashed curves) due to the high shear. Model results shown here for clear fluid flow are consistent with prior numerical studies on oscillatory bottom boundary layer using a standard  $k - \epsilon$  closure [e.g., Justesen, 1988]. Numerical results further suggest that when fluid-mud is present (solid curves), turbulent intensity very near the bed ( $z < 2 \text{ cm}$ ) is attenuated comparing to that of clear fluid condition. This reduction of turbulence is mainly caused by the viscous drag term in the  $k - \epsilon$  equations. Near and above the lutocline, reduction of turbulent intensity is also observed, which is mainly caused by sediment density stratification. Because of the gradient transport assumption (see section 2.2.1), the sediment density stratification term in the  $k$ -equation is parameterized as proportional to the eddy viscosity. Hence, model results indicate that sediment density stratification is of less importance in attenuating carrier flow turbulence as compared to viscous drag very close to the bed, especially when sediment concentration becomes large.

[38] It is also noted that in the middle portion of the wave boundary layer, the turbulent intensity is noticeably larger when the fluid-mud is present. Despite the fact that the presence of sediment can directly damp carrier flow turbulence, the effect of sediment rheological stress in this case effectively enhances the wave boundary layer thickness and hence the boundary layer turbulence must also increase accordingly (i.e. turbulent intensity scales with boundary layer thickness). For the present moderate magnitude of sediment concentration ( $10\text{--}60 \text{ g l}^{-1}$ ) and Newtonian rheological stresses, model results suggest that the flow in the fluid mud layer remains turbulent. Thus, the fluid-mud thickness is related to the suspension capacity of the flow field. On the other hand, as the fluid mud concentration becomes as large as  $100$  to  $200 \text{ g l}^{-1}$ , the flow in the fluid mud layer may be significantly retarded by the rheological

stress (i.e. thixotropic) and become laminar. Under such condition, field observations also suggest that strong interfacial wave features may appear (P. Traykovski, personal communication, 2008).

[39] Numerical results presented in Figure 3 reveal a possible scaling relationship between the wave boundary layer thickness  $\delta$  and the fluid-mud layer thickness  $d$ . Although there is a lack of detailed observations of the wave boundary structure inside the fluid mud layer, this scaling has been suggested by some authors [e.g., Vinzon and Mehta, 1998; Traykovski et al., 2000] based on (limited) observations. In order to show such a scaling relationship, another simulation is carried out where the rheology coefficient  $\nu_{s0}$  is reduced, while the wave characteristics and the rest of parameters remain unchanged (case 1C). Figure 4 shows the horizontal velocity and mass concentration profiles for the high and low rheology cases at the maximum free-stream velocity phase. As  $\nu_{s0}$  is reduced, a thinner fluid-mud layer with a higher near bed concentration (with respect to case 1A) is observed. As shown in Figure 4b, the fluid-mud layer thickness is also sensitive to the criteria to determine the lutocline location, resulting in larger values when the  $10 \text{ g l}^{-1}$  threshold is employed. However, consistent with both definitions, it can be observed that the wave boundary layer (distance from the bottom to the near bed maximum velocity in Figure 4a) scales with the fluid-mud layer thickness in these two cases.

[40] To further explore this scaling and its parameterization, the following formulation is used to obtain an estimate of the wave boundary layer thickness based on the near bed flow conditions [e.g., Gant and Madsen, 1979]

$$\delta_1 = \frac{\gamma U_*}{\sigma}, \quad (21)$$

where the friction velocity  $U_*$  in (21) is calculated in this study by considering both rheological  $\tau_b^s$  and fluid  $\tau_b^f$  bottom stresses. Adopting  $\gamma = 0.74$ , given by the best-fit of (21) to  $d$  of the cases with the same rheology and erodibility coefficients (cases 1A, 1D, and 1E), the values of  $\delta_1$  as predicted via (21) in all the monochromatic wave simulations are plotted against the fluid-mud layer thickness given by definition (II) (Figure 5). Detailed values of the model observations and predictions of the ratio  $d/\delta$  are also presented in Table 2. A generally good scaling relation between the wave boundary layer and the fluid-mud layer thickness is shown for most of the simulated tests (Figure 5). Specifically, for a given set of rheological and erodibility parameters, a very good scaling relation remains for different wave amplitudes (cases 1A, 1D and 1E). However, as the rheological stress becomes smaller (mud becomes less viscous, Figure 5, case 1C) or the erodibility is reduced (more consolidated mud bed, cases 1G and 1H), the discrepancies become larger. Thus, the value of  $\gamma$  (dependent on  $\kappa$ ) in (21) may be changed accordingly to the fluid-mud properties.

[41] Overall, model results suggested the possibility to estimate the fluid mud layer thickness using (21). The success of this parameterization relies in that  $U_*$  includes information of the mud rheological stress  $\tau_b^s$  near the bed. This result may be of particular relevance for inferring near bed mud layer characteristics based on the wave observations [e.g., Rogers and Holland, 2009].

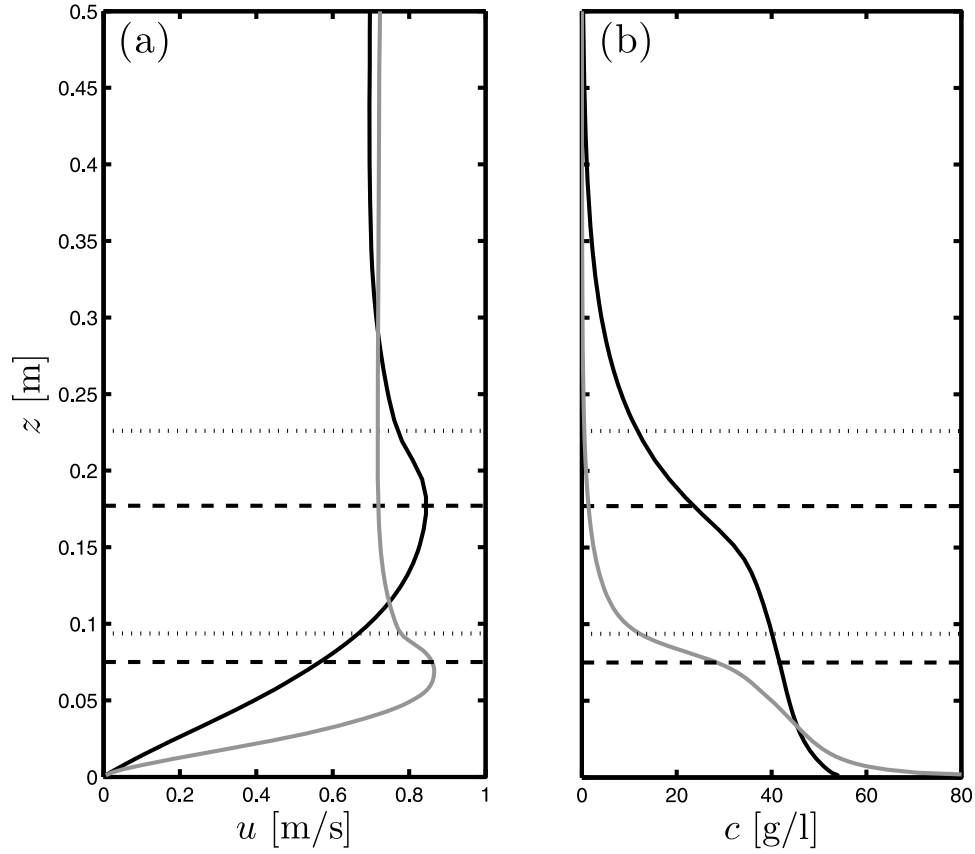


**Figure 4.** Instantaneous (a) horizontal velocity and (b) mass concentration profiles for the high- (black solid curve) and low- (gray solid curve) rheology cases (cases 1A and 1C, respectively). The horizontal lines denote the time-averaged fluid-mud layer thickness according with the two different definitions: (I) the location of the  $10 \text{ g l}^{-1}$  concentration threshold (dotted lines) and (II) maximum concentration gradient (dashed lines).

### 3.2. Water-Wave Dynamics

[42] As previously shown, the numerical model predicts the expected wave amplitude attenuation at the downstream end of the numerical flume (Figure 2). This wave energy attenuation is caused by the rheological stress, i.e. the enhanced sediment effective viscosity of the concentrated mud flow. The lack of a comprehensive experiment, with detailed in-situ observations on boundary layer velocity, sediment concentration, floc properties, rheological and erodibility parameters prevents us from carrying out a more realistic model-data comparison. On the other hand, the classic two-layer approach has been utilized and verified in many prior studies and more importantly it adopts several well-defined model assumptions, such as small amplitude waves.

#### 3.2.1. Mud-Induced Primary Wave Dissipation

[43] In this study a systematic model verification with the semi-analytical solution of a two-layer model is carried out in order to demonstrate the self-consistency of the more complicated numerical model. This model verification consists of using the numerical model as a virtual laboratory, which provides detailed spatial and temporal flow information of the fluid mud layer and the wave attenuation across the flume for a given set of wave condition, and rheology and erodibility parameters. Numerical model

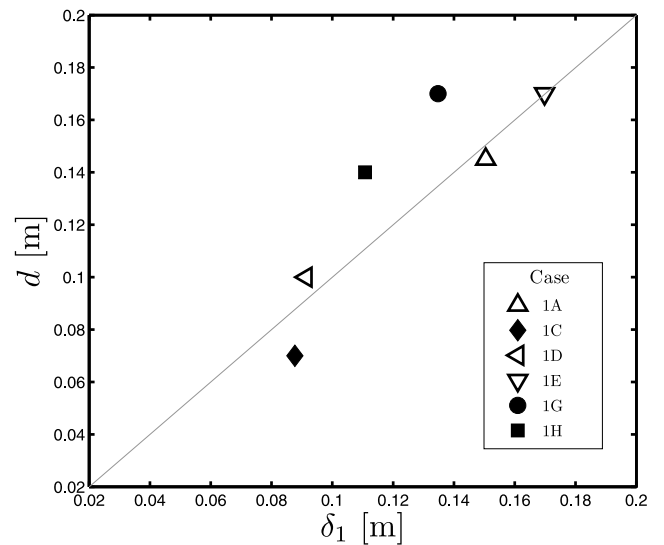


**Figure 5.** Scaling between the estimated wave boundary layer thickness  $\delta_1$  and the fluid-mud thickness (definition II) for all (monochromatic) simulated cases.

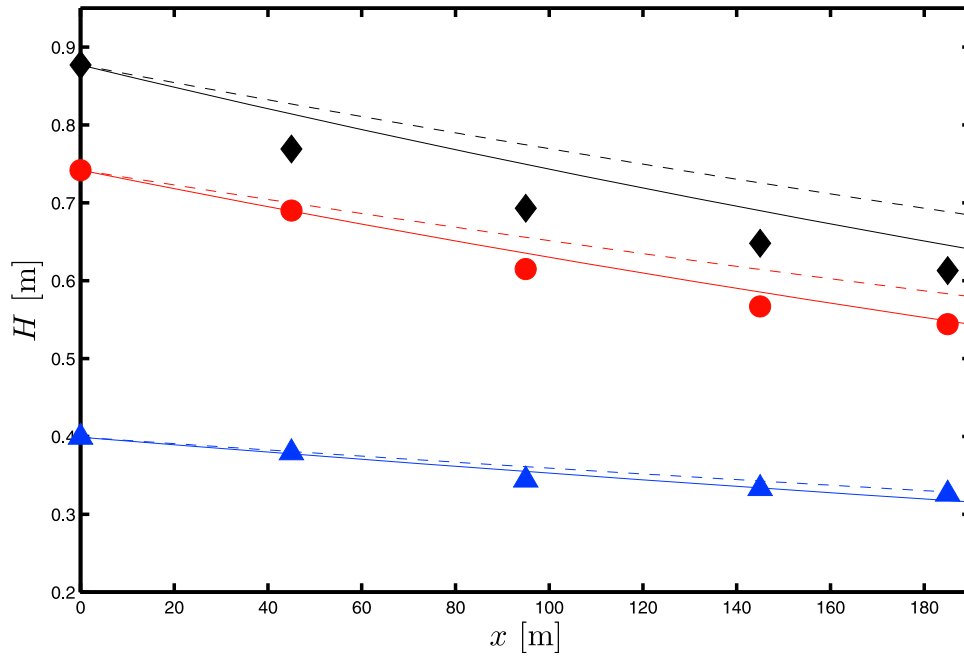


**Figure 6.** Wave height variation across a muddy seabed as observed in the nonlinear model (symbols) and predicted by the two-layer model employing two different definitions of the fluid-mud thickness (dashed curve is definition I, solid curve is definition II).

results at the mid-flume position ( $x = 100$  m in Figure 2) are depth and time integrated in order to calculate fluid-mud bulk parameters, i.e.  $\nu_m$  and  $\rho_m$ , as

$$\nu_m = \int_0^d \int_{T_{N-1}}^{T_N} \nu(x, z, t) dz dt \quad \text{and} \quad \rho_m = \int_0^d \int_{T_{N-1}}^{T_N} \rho(x, z, t) dz dt \quad (22)$$

where the time integration covers the last wave period  $T_N$  (after quasi-stationary results are obtained) where  $N$  is the total number of waves in the simulation (i.e., thirty), whereas the upper limit in the depth- integration is given by the fluid-mud layer thickness  $d$ . Finally, the computed bulk flow quantities are used together with the incident wave parameters ( $H$  and  $T$ ) to drive the two-layer model of *Dalrymple and Liu* [1978] [see also *Kranenburg*, 2008]. Three progressive wave tests employing the same rheology and erodibility parameters but different values of wave amplitude (cases 1A, 1D, and 1E) are considered. Notice that the bulk mud parameters  $\nu_m$  and  $\rho_m$  are sensitive to the adopted definition of  $d$  (see Table 3). Therefore, the two definitions mentioned in section 3.1 are both utilized here to drive the two-layer model. The dissipation (attenuation) rate is computed as

$$\mathcal{D} = \frac{dF/dx}{F} = -2\text{Im}(k_w), \quad (23)$$

where  $F$  is the energy flux, and  $k_w$  is the (imaginary) wave number (used in the two-layer model). The wave height predicted using the two-layer model is compared with the (model) observations at different cross-shore locations (see Figure 6). A summary of bulk parameters computed from

the numerical model results, as well as observed (numerical model) and predicted (two-layer model) dissipation rates are presented in Table 3.

[44] The present continuous numerical model and the two-layer model predict very similar decay rate of the wave amplitude as small amplitude waves propagate downstream independently of the fluid-mud definition employed (Figure 6). However, a better overall agreement (all cases) between the numerical model results and two-layer model results is obtained when using the maximum vertical concentration gradient (definition II) to define the top of the fluid mud layer and to calculate the required parameters for the two-layer model (see Table 3 (definition II) and Figure 6, solid curves). Despite some expected differences between the two models for the more energetic condition (case 1E), the agreement is still satisfactory using (II). On the other hand, larger discrepancies for the more energetic wave conditions (case 1A and 1E) can be observed between the numerical results and the two-layer model predictions when using the threshold in mass concentration (i.e.  $10 \text{ g l}^{-1}$ ) to estimate input parameters (Table 3 (definition I) and Figure 6, dashed curves). As shown in Figure 4b, for the cases modeled in this study, the definition (II) often locates the lutocline closer to the bed where the sediment mass concentration is about two to three times greater than  $10 \text{ g l}^{-1}$  and the rheological stress is still significant (see Figure 3e). It also can be observed from Figure 4 that sediment concentration below this location is indeed more uniform (and concentrated) and hence is more consistent with the layered flow assumption adopted in the two-layer model formulation. Hence, we believe that using the maximum vertical concentration gradient to define the top of the mud layer thickness is a more dynamic definition of the fluid mud layer thickness for the two-layer model. In the study of two-

**Table 3.** Summary of Fluid-Mud Bulk Parameters Derived by the Nonlinear Model and Dissipation Rates Predicted by Both Nonlinear  $\mathcal{D}_{obs}$  and Two-Layer  $\mathcal{D}_{pred}$  Models

Case	$d$ (m)	$\nu_m$ (m <sup>2</sup> s <sup>-1</sup> )	$\rho_m$ (Kg m <sup>-3</sup> )	$\delta_2 = \sqrt{2\nu_m/\sigma}$	$d/\delta_2$	$\mathcal{D}_{obs}$ (m <sup>-1</sup> )	$\mathcal{D}_{pred}$ (m <sup>-1</sup> )
<i>Fluid-Mud Thickness According to Definition I</i>							
1A	0.21	0.0022	1021	0.065	3.24	0.0034	0.0026
1D	0.13	0.0014	1019	0.052	2.42	0.0022	0.0020
1E	0.25	0.0022	1021	0.065	3.85	0.0038	0.0026
1G	0.185	0.0015	1020	0.054	3.55	0.0014	0.0011
<i>Fluid-Mud Thickness According to Definition II</i>							
1A	0.15	0.0031	1026	0.077	1.95	0.0034	0.0032
1D	0.10	0.0017	1021	0.057	1.75	0.0022	0.0024
1E	0.17	0.0033	1026	0.079	2.14	0.0038	0.0034
1G	0.17	0.0016	1021	0.055	3.08	0.0014	0.0011

layer model, the Stokes wave boundary layer thickness  $\delta_2 = \sqrt{2\nu_m/\sigma}$ , where  $\sigma = 2\pi/T$  is the wave angular frequency, is often used. As presented in Table 3 (definition II), model results suggest that for small amplitude waves (case 1D) the numerical model is consistent with two-layer theory which predicts a maximum dissipation ratio  $d/\delta_2$  close to 1.6. However, more energetic simulations (1A and 1E) revealed an increasing magnitude of this ratio with increasing wave nonlinearity, departing from the ratio of maximum dissipation predicted by two-layer models. Using the same wave conditions than in Test 1A, the model is driven prescribing a homogenous fluid-mud layer, i.e., constant fluid-mud viscosity and density (concentration) through the water column. Consistent with analytical results, the bulk dissipation rate is not too sensitive to the vertical variation for the sediment concentrations reported here (<50 g/l). Thus, differences between the two models can be ascribed to the nonlinear effects due to having finite amplitude. Notice that the effect of having nonuniform fluid mud characteristics may become important for a more complex rheological closure and higher sediment concentration (>100 g/l) not addressed in the present investigation.

[45] We investigate the effect of sediment supply limitation in the numerical model by decreasing the sediment erodibility (case 1G.) The resulting fluid-mud layer is more dilute (i.e.,  $\nu = 1.6 \times 10^{-3}$  m<sup>2</sup> s<sup>-1</sup> and  $d = 0.17$  m) than under high erodibility conditions (i.e. case 1A) and hence the dissipation rate is lower in the former scenario (see Table 3 (definition II). Also, for this specific case the two-layer model dissipation rate is independent on the fluid-mud thickness definition employed (see case 1G in Table 3). As shown in Table 3 (definition II), the (nonlinear) numerical model suggests that the ratio does not adjust itself to the ratio of maximum dissipation in two-layer models (i.e.,  $d/\delta_2 = 1.6$ ). Differences with respect to this ratio are larger for increasing nonlinearity and/or decreasing sediment supply. Based on these results, the two-layer model application for the inverse problem [e.g., Rogers and Holland, 2009] fails for energetic waves propagating over a small concentration sediment suspension (e.g., pre-storm conditions).

[46] Inter-model comparison shown here provides confidence in the numerical model consistency with respect to simplified models. Moreover, some of the trends observed in the field seems to be at least qualitatively reproduced by the model. Although we have to take cautiously the numerical results of this study due to limited model validation against measured data, the numerical model at this

point can help providing evidences in identifying some of the key mechanisms of wave attenuation.

### 3.2.2. High-Frequency Wave Attenuation

[47] Another topic of interest is the unexpected short-wave attenuation reported from field observations in the inner shelf of Louisiana [e.g., Sheremet and Stone, 2003]. A recent study using a frequency-domain nonlinear wave model incorporating the mud dissipation effect through a two-layer approach [Kaihatu et al., 2007] demonstrates that the damping of short-waves ( $kh > 3.0$ ) is mediated by triad interactions.

[48] Following Kaihatu et al. [2007], the wave attenuation along the different phase-locked harmonics (e.g.  $f_1, f_2, f_3$ ) is investigated using the present cnoidal wave simulation results. The amplitudes at discrete frequencies for both the clear fluid (case 1B) and the fluid-mud (case 1A) simulations are computed at the downstream end of the numerical wave flume ( $x = 185$  m). Consistent with recent findings [e.g., Kaihatu et al., 2007], the higher attenuation rates correspond to the higher frequencies in the spectra where waves are in the range of relatively deep water (see Figure 7). Some authors [e.g., Sheremet et al., 2005] have hypothesized that this energy loss is mediated by the nonlinear energy transfer to lower frequencies, which are able to interact with the fluid-mud layer directly. A more detailed analysis of the role of wave-wave interaction on explaining the frequency-dependent attenuation rate at low-frequencies will be presented in the next section 3.2.3.

[49] We also carry out another clear fluid simulation for the same wave conditions but using a very large bottom roughness (case 1F) with two main objectives. First, we like to isolate the nonlinear interaction corresponding to the surface wave-wave system from the possible interaction between the bottom mud transport (e.g. lutocline waves) and the surface waves. Secondly, it is of interest to evaluate the possibility of using a simple approach, such as drastically enhanced bottom roughness, to parameterize the fluid-mud effects on wave attenuation. Such parameterization is very useful for large-scale wave propagation models [e.g., Winterwerp et al., 2007; Rogers and Holland, 2009]. The  $K_s$  value used for case 1F is chosen by trial an error in order to match the observed wave amplitude at the downstream end of the flume in the fluid-mud simulation (case 1A). Numerical model results suggest that the large roughness case also reproduces quite well the amplitude attenuation along the different frequency components (Figure 7). Therefore, for the present wave condition and moderate

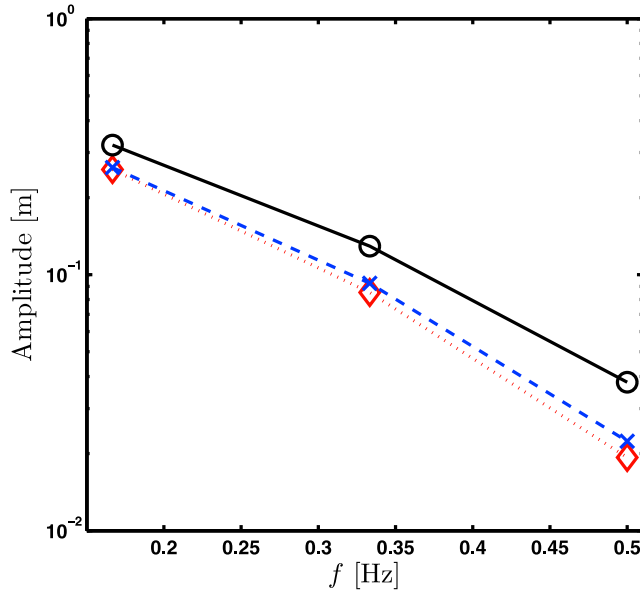


**Figure 7.** Amplitude for discrete frequencies at  $x = 180$  m for: clear fluid (case 1B; circles), fluid-mud (case 1A; crosses), and large roughness (case 1F; diamonds).

concentration of fluid mud, wave-wave interaction is responsible for most of the amplitude attenuation occurring at very high frequencies. Small differences between the fluid-mud and the large roughness simulations in the second- and third- harmonics can be ascribed to additional nonlinear interaction between the fluid-mud and the surface waves which cannot be accounted for in the large roughness simulation. Interestingly, the numerical model results also suggest that the maximum bottom shear stress  $\tau_b^f$  caused by the enhanced bottom roughness in case 1F is of similar magnitude to the total bottom stress ( $\tau_b^f + \tau_b^s$ ) in the fluid-mud simulation (case 1A). This may imply that the direct wave dissipation mechanism due to viscous fluid mud can be well parameterized by an enhanced roughness that matches the total bottom stress.

### 3.2.3. Low-Frequency Wave Attenuation

[50] The role of nonlinear wave-wave interaction in explaining the mud-induced frequency-dependent dissipation rate [e.g., *Kaihatu et al.*, 2007; *Elgar and Raubenheimer*, 2008] is addressed in this section by means of wave group (bichromatic) simulations at intermediate (constant) water depth using the numerical model (case 2A). Confidence in the model results is provided by a prior study which demonstrated the model capability for simulating the lf-wave transformation during shoaling and breaking of irregular waves on an impermeable seabed [*Torres-Freyermuth et al.*, 2010]. The attenuation rates are computed at the downstream end of the numerical wave flume based on the energy flux difference with respect to a clear fluid simulation (case 2B). The numerical model is further employed to carry out another two clear fluid simulations but with greatly enhanced bed roughness (cases 2C and 2D) in order to investigate the possible parameterization of the frequency-dependent wave attenuation due to muddy seabed and to corroborate the hypothesis drawn from the fluid-mud results.

[51] A second-order wave generation procedure is employed in order to include the bound-harmonics ( $f_2 - f_1$  and  $f_2 + f_1$ ) associated to the primary components ( $f_1$  and  $f_2$ ). This is particularly important when an accurate analysis of the frequency dependent (energy) attenuation rates is sought. The (second-order) incident wave spectrum is computed using *Longuet-Higgins and Stewart* [1960, hereafter LH&S60]. This approximation is expected to hold up to intermediate water depths ( $0.5 < kh$ ). On the other hand, at the downstream end of the numerical wave flume, an open (radiation) boundary condition is implemented to allow the incoming waves to propagate outside of the computational domain without (or with minimum) reflection. Figure 8 shows the computed free-surface elevation at the downstream end of the flume due to a bichromatic wave train propagating over 200 m in the numerical wave flume of 2.5 m water depth employing the open boundary (case 2B, clear fluid flow). Both the numerically computed lf-wave (solid curve, obtained as the low-passed filtered free-surface elevation signal at the downstream end of the numerical

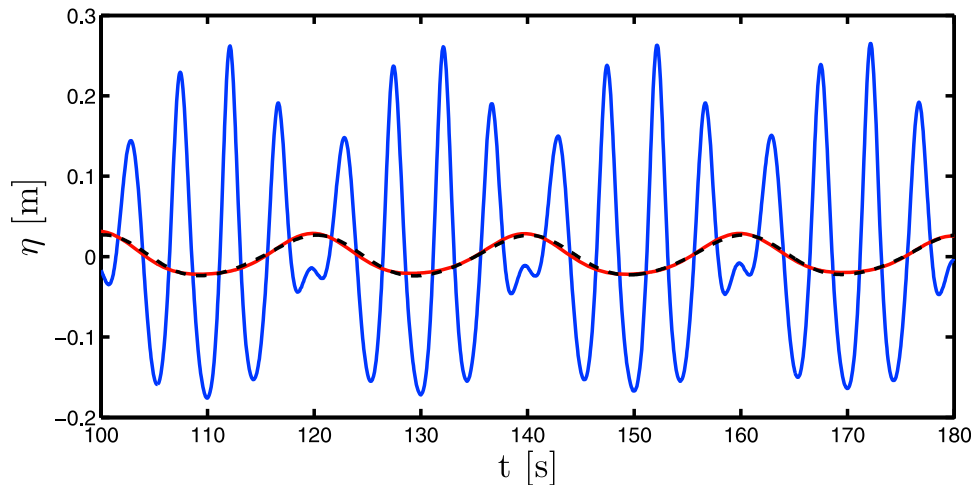


**Figure 8.** Short- and bound-wave ( $\times 2$ ) as measured (solid curve is the low-passed signal) predicted (dashed curve is from LH&S60) at the downstream end of the numerical flume.

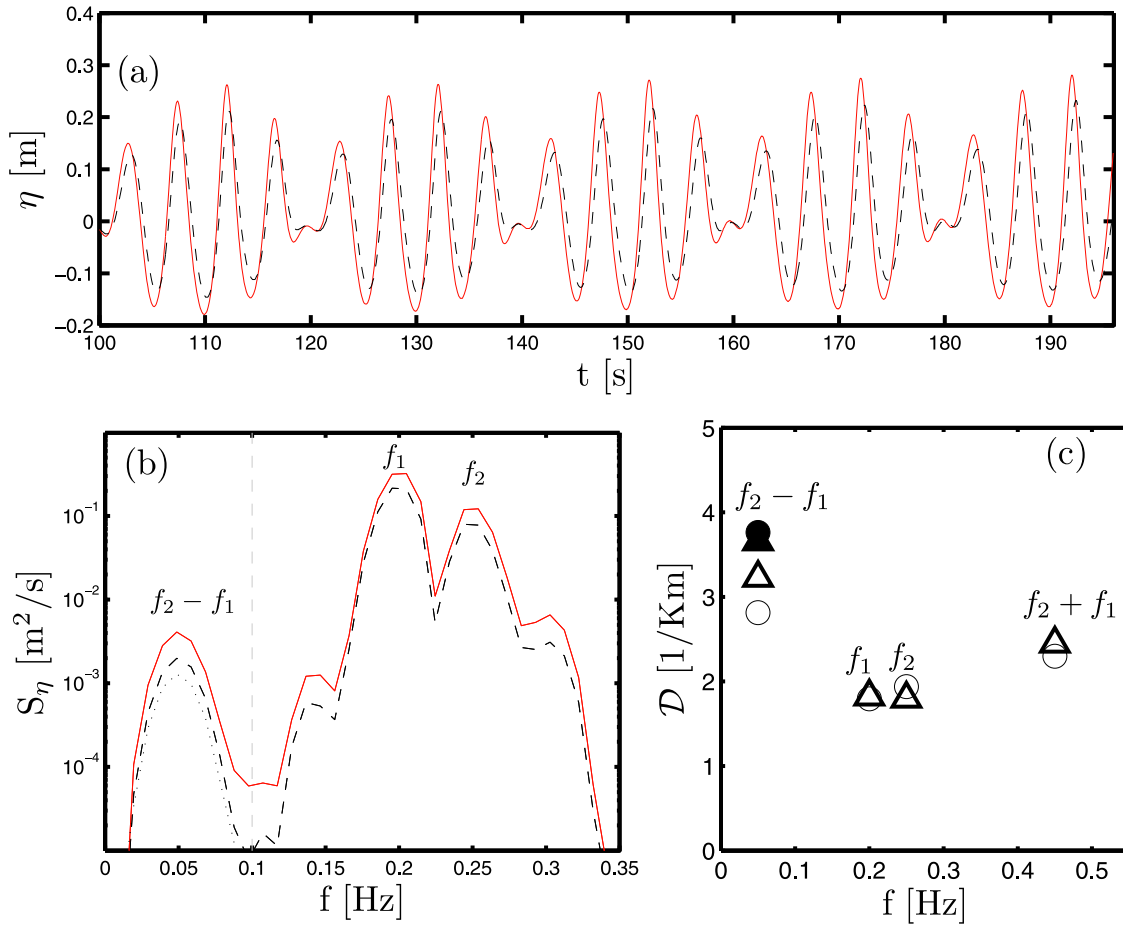


**Figure 9.** (a) Free-surface elevation time series measured at the downstream of the flume ( $x = 185\text{m}$ ) for the clear fluid (red curve) and the fluid-mud (black dashed curve) simulations. (b) Free-surface energy density spectra for these two simulations and the LH&S60 (dotted curve). Differences between the nondissipative (solid curve) and dissipative (dashed curve) cases are attributed to fluid-mud induced dissipation. (c) Dissipation rate at discrete frequencies obtained for cases 2A (circles) and 2B (triangles). The dissipation rates are higher for the subharmonic ( $f_2 - f_1$ ) frequency (solid symbols are from LH&S60 second-order solution, open symbols are simulated).

wave flume) and the theoretical bound-wave calculated via LH&S60 (dashed curve) are in good agreement in both amplitude and phase. This implies that: (i) the open boundary condition can effectively absorb both incoming short- and long- waves, and (ii) the LH&S60 second-order theory provide a good estimate of the bound long-wave in this case.

### 3.2.3.1. Muddy Seabed

[52] A wave group with bound-harmonics included is sent into the numerical wave flume and two numerical experiments, one with mud suspended (case 2A, near bed mud concentration  $50 \text{ g l}^{-1}$ ) and the other reference case of clear fluid flow (case 2B), are carried out. Free-surface elevation time histories measured at the downstream end of the flume show a decay of wave amplitude due to fluid-mud (Figure 9a). The energy attenuation occurs among all frequencies in the energy spectrum (Figure 9b). Differences between numerical model results with mud transport (denoted as dissipative, dashed curve) and without mud transport (denoted as nondissipative, solid curve) are attributed to mud-induced dissipation. Following *Elgar*

and *Raubenheimer* [2008], the frequency-dependent dissipation (attenuation) rate  $\mathcal{D}$  at discrete frequencies is obtained by comparing the energy flux computed by the numerical simulations (clear fluid vs fluid-mud) at the same cross-shore location (i.e.  $x = 185 \text{ m}$ ) using

$$\mathcal{D}(x) = \frac{(F(x)_{nd} - F(x)_d)/x}{F(x)_{nd}} \quad (24)$$

and

$$F(x) = \rho^f g \int_{f_L}^{f_U} S(x, f) c_g(x, f) df, \quad (25)$$

where  $S(x, f)$  and  $c_g(x, f)$  are the free-surface spectral density and group velocity, respectively, whereas subscripts  $d$  and  $nd$  denotes dissipative (cases 2A, 2C, and 2D) and nondissipative (case 2B) conditions. The energy flux is computed using (25), where the lower  $f_L$  and upper  $f_U$  integration limits are given by  $f_L = 0.03, 0.1, 0.225$ , and



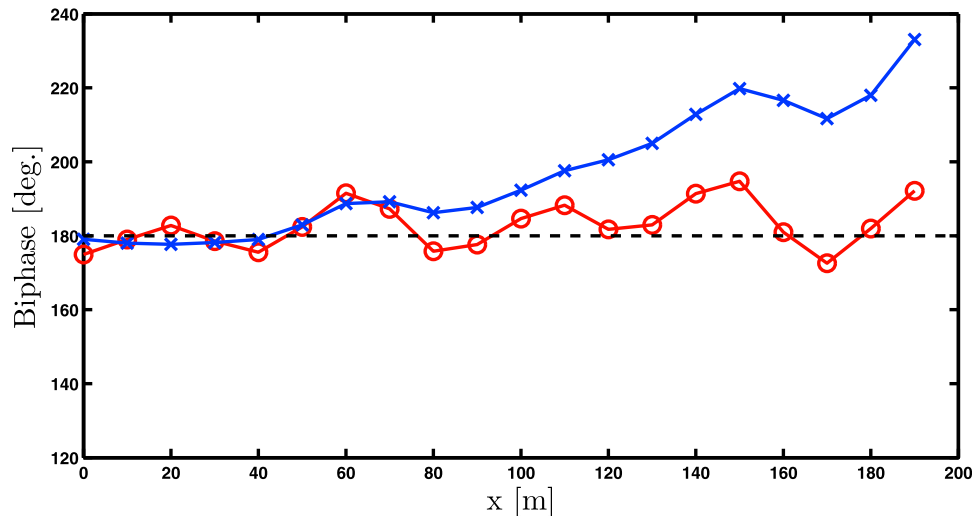


**Figure 10.** Biphase between the difference interaction ( $f_2 - f_1$ ) and the peak frequency ( $f_1$ ) along the numerical wave flume for clear fluid with smooth (circles) and rough (crosses) seabeds.

0.35 Hz and  $f_U = 0.1, 0.225, 0.35$ , and 0.60 Hz. The higher dissipation rates for this case correspond to the bound-harmonics (see Figure 9c). Notice that the dissipation rates for the principal frequency components ( $f_1 = 0.20$  and  $f_2 = 0.25$  Hz) are quite similar. It is important to highlight that most of the energy is concentrated around these frequencies, which account for  $\approx 97\%$  of the total energy variance. From here on the analysis will be focused on explaining the high attenuation rate occurring at the low frequency (lf) mode (i.e., difference interaction  $f_2 - f_1$ ).

[53] The attenuated spectrum, measured at the downstream end of the flume, is band-passed filtered ( $0.1 < f < 0.3$  Hz) and is used to compute the lf bound-wave ( $f < 0.1$  Hz) according to LH&S60. As shown in Figure 9b, the theoretical lf-wave (dotted curve) slightly underestimated the lf-energy observed in the simulation. The good agreement with second-order wave theory for this case suggest that the mud-induced energy dissipation is (mainly) occurring at the primary wave components and hence the observed (high) attenuation rate at low frequencies results from the energy redistribution within the spectrum in order to achieve the dynamical equilibrium. For completeness, the lf-wave dissipation rate based on the second-order solution is also plotted in Figure 9c (solid circle).

### 3.2.3.2. Rough Seabed

[54] The presence of the fluid-mud and the complexity of its behavior (i.e., rheology) may obscure the interpretation of the frequency-dependent attenuation rate function previously obtained. For instance, it is difficult to identify to what extend the lf-wave energy attenuation is triggered by the fluid mud transport processes. Specifically, it is not straightforward to conclude that the lf-wave energy attenuation is due to the direct interaction with the bottom fluid-mud layer processes or if it is simply the responsive effect of the dissipation occurring at the primary frequencies (as suggested above). Therefore, similar to monochromatic wave condition, we carry out additional simulations using enhanced bottom roughness with clear fluid flow (without mud) for wave group.

[55] The numerical setup previously described is employed again for clear fluid flow simulation with a larger  $K_s$  value employed in the bottom boundary condition (see equation (17); sediment transport module turned off). At the end of section 3.2 it was found that as  $K_s$  is increased, the fluid friction velocity  $u_*$  required to match the amplitude attenuation observed in the fluid-mud simulation was very similar to the total friction velocity  $U_*$  for the fluid-mud case. Hence, the bottom roughness is chosen here in order to approximately match  $u_*$  with the  $U_*$  observed in case 2A at a given cross-shore location (e.g.  $x = 40$  m). Following the analysis presented in section 3.2.3.1, the attenuation rates for enhanced  $K_s$  computed using (24) shows good agreement with the fluid-mud simulation (see Figure 9c compare circles with triangles). Numerical results with enhance  $K_s$  also captures the larger attenuation rates at bound-wave frequencies. Moreover, good agreement with the second-order wave theory is also observed for the (lf) bound-wave (compare open- and solid-triangles). Therefore, the nonlinear (surface) wave interaction seems to be the predominant lf-wave attenuation mechanism for the fluid-mud concentration and rheology considered in this work.

[56] A time domain analysis of cases 2A and 2C show a small phase lead (with respect to  $180^\circ$ ) between the lf-wave and the short-wave envelope at the downstream end of the flume (not shown), implying that energy transfer between components is taking place. In order to further study this process, an extreme scenario is simulated (case 2D) where the roughness height is further increased (see Table 3). In this highly dissipative case the difference in phase between measured and predicted lf-wave becomes significant. Contrary with the well-known phase lag (biphase  $< 180^\circ$ ) between the lf-wave and the short-wave envelope during wave shoaling [e.g., *Elgar and Guza*, 1985; *van Dongeren*, 1997; *Battjes et al.*, 2004], a bispectrum analysis [e.g., *Elgar and Guza*, 1985] of the numerical results revealed a (lf-wave) phase lead (biphase  $> 180^\circ$ ) in case 2D (see Figure 10) whereas the nondissipative simulation (case 2B) oscillates around the equilibrium value of  $180^\circ$ . The former result implies that the energy is transferred from the lf- toward the



sea-swell band being consistent with the aforementioned hypothesis. The energy transfer is triggered by the energy dissipation occurring at the primary components ( $f_1$  and  $f_2$ ).

[57] In summary, numerical results revealed that the direct mud-induced dissipation occurs (mainly) at the primary (i.e., sea-swell) components (able to put the sediment into suspension) where the mud rheological effect (dependent on the strain-rate values) is stronger. This energy dissipation at the primary frequencies produces a phase-lead between the bound wave and the short-wave envelope, triggering the energy transfer towards the primary wave components in order to try to reach the equilibrium state [e.g., *Longuet-Higgins and Stewart*, 1962]. This energy re-distribution in the spectrum is similar to the inverse shoaling effect. Thus, the proportionality between the primary waves dissipation and the corresponding energy transfer from lf waves to spectral peak results in this high normalized dissipation rate for lf-waves. The lf-wave dissipation mechanism is conceptually the opposite of the one presented by *Elgar and Raubenheimer* [2008]. Nevertheless, a direct comparison between the two works is not possible since the shoaling effect, considered by *Elgar and Raubenheimer* [2008], is not incorporated in the present model results. The numerical results suggest that, for intermediate (constant) water depth and moderate concentration of the fluid mud, the frequency-dissipation function can be explained from the wave problem perspective alone (if the dissipation is gradual enough), implying that our wave-mud interaction modeling effort can be devoted to find out the right parameterization for wave dissipation occurring at the principal wave components able to erode the seabed. However, a more complex situation is foreseen when the wave propagates over a sloping highly concentrated fluid-mud layer in shallow waters [e.g., *Elgar and Raubenheimer*, 2008]. Thus, this topic deserves further research and requires the use of field/laboratory observations to validate/extend this hypothesis.

#### 4. Conclusions

[58] A new modeling framework for fine sediment transport (mixture approach), derived based on the Equilibrium Eulerian method, provides a mean to study wave-mud interaction processes continuously and consistently by a single set of two-dimensional equations and closures. Numerical results reveal an enhancement of the wave boundary layer due to rheological stresses. The enhanced wave boundary (viscous) layer scales with the fluid-mud layer, whereas the wave amplitude is directly dissipated by the rheological stress. The numerical model is in agreement with the two-layer model formulation for low energy conditions when top of the fluid-mud layer is defined by the maximum vertical concentration gradient. On the other hand, the two-layer formulation is not able to reproduce the dissipation rate under more energetic conditions. The latter may be ascribed to the two-layer limitations implicit in its derivation. Also, the numerical model confirmed the importance of nonlinear wave interaction in explaining the energy attenuation occurring at high- and low-frequency waves. Moreover, it is also shown that at intermediate (constant) water depth the wave dissipation rate at the principle harmonics is similar while the higher and lower harmonics present larger attenuation rates, consistent with

second-order theory estimates for the band-passed signal. Furthermore, the bispectrum analysis confirmed that the lf-wave attenuation (mainly) occurs due to the energy transfer from low-frequencies toward the principal components where energy is directly dissipated. Nevertheless, the lack of a proper model validation restricts the current investigation to a qualitative level. Thus, it is important to validate the turbulence model for low concentration conditions before addressing the modeling of highly concentrated fluid-mud which develops a more complex rheological behavior. Future work will be considered to study the effect of the sloping bottom in the mud-induced frequency dependent energy attenuation.

[59] **Acknowledgments.** This study is supported by Office of Naval Research (N00014-09-1-0134) and National Science Foundation (OCE-0913283). Torres-Freyermuth also wish to acknowledge partial financial support provided by the Department of Civil and Environmental Engineering, University of Delaware and CONACYT (M0023-08-06-106400 and 10007-09-1-116901).

#### References

- Amoudry, L., T. J. Hsu, and P. L.-F. Liu (2008), Two-phase model for sand transport in sheet flow regime, *J. Geophys. Res.*, **113**, C03011, doi:10.1029/2007JC004179.
- Battjes, J. A., H. J. Bakkenes, T. T. Janssen, and A. R. van Dongeren (2004), Shoaling of subharmonic gravity waves, *J. Geophys. Res.*, **109**, C02009, doi:10.1029/2003JC001863.
- Booij, N., R. C. Ris, and L. H. Holthuijsen (1999), A third generation wave model for coastal regions: 1. Model description and validation, *J. Geophys. Res.*, **104**, 7649–7666.
- Campbell, C. S. (1990), Rapid granular flow, *Ann. Rev. Fluid Mech.*, **22**, 57–92.
- Cantero, M. I., S. Balachandar, A. Cantelli, C. Pirmez, and G. Parker (2009), Turbidity current with a roof: Direct numerical simulation of self-stratified turbulent channel flow driven by suspended sediment, *J. Geophys. Res.*, **114**, C03008, doi:10.1029/2008JC004978.
- Carpen, I. C., and J. F. Brady (2002), Gravitational instability in suspension flow, *J. Fluid Mech.*, **472**, 201–210.
- Chan, I.-C., and P. L.-F. Liu (2009), Responses of Bingham-plastic muddy seabed to surface solitary wave, *J. Fluid Mech.*, **618**, 155–180.
- Dalrymple, R. A., and P. L.-F. Liu (1978), Waves over soft muds: A two-layer fluid model, *J. Phys. Oceanogr.*, **8**, 1121–1131.
- De Wit, P. J. (1995), Liquefaction of cohesive sediment by waves, Ph.D. thesis, Delft Univ. of Technol., Delft, Netherlands.
- Drew, D. A. (1983), Mathematical modeling of two-phase flow, *Ann. Rev. Fluid Mech.*, **15**, 261–291.
- Dyer, K. R. (1989), Sediment processes in estuaries: Future research requirements, *J. Geophys. Res.*, **94**(C10), 14,327–14,339.
- Elgar, S., and R. T. Guza (1985), Shoaling gravity waves: Comparisons between field observations, linear theory, and nonlinear model, *J. Fluid Mech.*, **158**, 47–70.
- Elgar, S., and B. Raubenheimer (2008), Wave dissipation by muddy sea-floors, *Geophys. Res. Lett.*, **35**, L07611, doi:10.1029/2008GL033245.
- Elghobashi, S. E., and T. W. Abou-Arab (1983), A two-equation turbulence model for two-phase flows, *Phys. Fluids*, **26**, 931–938.
- Ferry, J., and S. Balachandar (2001), A fast Eulerian method for disperse two-phase flow, *Int. J. Multiphase Flow*, **27**, 1199–1226.
- Foda, M. A., J. R. Hunt, and H.-T. Chou (1993), A nonlinear model for the fluidization of marine mud by waves, *J. Geophys. Res.*, **98**(C4), 7039–7047.
- Forristall, G. Z., and A. M. Reece (1985), Measurements of wave attenuation due to a soft bottom: The SWAMP experiment, *J. Geophys. Res.*, **90**, 3367–3380.
- Frigaard, I. A., and C. Nouar (2005), On the usage of viscosity regularisation methods for visco-plastic fluid flow computation, *J. Non-Newtonian Fluid Mech.*, **127**, 1–26.
- Gade, H. G. (1958), Effects of a nonrigid, impermeable bottom on plane surface waves in shallow water, *J. Mar. Res.*, **16**, 61–82.
- Gant, W., and O. S. Madsen (1979), Combined wave and current interaction with rough bottom, *J. Geophys. Res.*, **84**(C4), 1979–1808.
- Hagatun, K., and K. Eidsvik (1986), Oscillating turbulent boundary layer with suspended sediments, *J. Geophys. Res.*, **91**, 13,045–13,055.

- Harris, C. K., P. A. Traykovski, and W. R. Geyer (2005), Flood dispersal and deposition by near-bed gravitational sediment flows and oceanographic transport: A numerical modeling study of the Eel River shelf, northern California, *J. Geophys. Res.*, **110**, C09025, doi:10.1029/2004JC002727.
- Hsu, T.-J., and P. L.-F. Liu (2004), Toward modeling turbulent suspension of sand in the nearshore, *J. Geophys. Res.*, **109**, C06018, doi:10.1029/2003JC002240.
- Hsu, T.-J., J. T. Jenkins, and P. L.-F. Liu (2003), On two-phase sediment transport: Dilute flow, *J. Geophys. Res.*, **108**(C3), 3057, doi:10.1029/2001JC001276.
- Hsu, T.-J., P. A. Traykovski, and G. C. Kineke (2007), On modeling boundary layer and gravity-driven fluid mud transport, *J. Geophys. Res.*, **112**, C04011, doi:10.1029/2006JC003719.
- Hsu, T.-J., C. E. Ozdeimir, and P. A. Traykovski (2009), High resolution numerical modeling of wave supported gravity-driven mudflows, *J. Geophys. Res.*, **114**, C05014, doi:10.1029/2008JC005006.
- Jaramillo, S., A. Sheremet, M. A. Allison, A. H. Reed, and K. T. Holland (2009), Wave-mud interactions over the muddy Atchafalaya subaqueous clinoform, Louisiana, USA: Wave-supported sediment transport, *J. Geophys. Res.*, **114**, C04002, doi:10.1029/2008JC004821.
- Jensen, B. L., B. M. Sumer, and J. Fredsøe (1989), Turbulent boundary layers at high Reynolds numbers, *J. Fluid Mech.*, **206**, 265–297.
- Justesen, P. (1988), Prediction of turbulent oscillatory flow over rough beds, *Coastal Eng.*, **12**, 257–284.
- Kaihatu, J. M., A. Sheremet, and K. T. Holland (2007), A model for wave propagation of nonlinear surface waves over viscous mud, *Coastal Eng.*, **54**, 752–764.
- Kineke, G. C., E. E. Higgins, K. Hart, and D. Velasco (2006), Fine-sediment transport associated with cold-front passages on the shallow shelf, Gulf of Mexico, *Cont. Shelf Res.*, **26**, 2073–2091.
- Kranenburg, C. (1994), The fractal structure of cohesive sediment aggregates, *Estuarine Coastal Shelf Sci.*, **39**, 451–460.
- Kranenburg, W. (2008), Modelling wave damping by fluid mud, M.Sc. thesis, Delft Univ. of Technol., Delft, Netherlands.
- Lamb, M. P., E. D'Asaro, and J. D. Parsons (2004), Turbulent structure of high-density suspensions formed under waves, *J. Geophys. Res.*, **109**, C12026, doi:10.1029/2004JC002355.
- Le Hir, P., P. Bassoulet, and H. Jestin (2001), Application of the continuous modeling concept to simulate high-concentration suspended sediment in a macro-tidal estuary, in *Coastal and Estuarine Fine Sediment Processes*, edited by W. H. McAnally and A. J. Mehta, Elsevier, Amsterdam.
- Lin, P., and P. L.-F. Liu (1998), A numerical study of breaking waves in the surf zone, *J. Fluid Mech.*, **359**, 239–264.
- Longuet-Higgins, M. S., and R. Stewart (1960), Change in the form of short gravity waves on long waves and tidal currents, *J. Fluid Mech.*, **8**, 565–583.
- Longuet-Higgins, M. S., and R. Stewart (1962), Radiation stress and mass transport in gravity waves with application to surf beats, *J. Fluid Mech.*, **13**, 481–504.
- Maa, P.-Y., and A. J. Mehta (1990), Soft mud response to water waves, *J. Waterw. Port Coastal Ocean Eng.*, **116**, 634–650.
- Maxey, M. R. (1987), The gravitational settling of aerosol particles in homogeneous turbulence and random flow fields, *J. Fluid Mech.*, **174**, 441–465.
- McPherson, H. (1980), The attenuation of water waves over non-rigid bed, *J. Fluid Mech.*, **97**(4), 721–742.
- Mehta, A. J. (1987), On estuarine cohesive sediment suspension behaviour, *J. Geophys. Res.*, **94**(C10), 14,303–14,314.
- Mei, C. C., and K.-F. Liu (1987), A Bingham-plastic model for a muddy seabed under long waves, *J. Geophys. Res.*, **92**(C13), 14,581–14,594.
- Ng, C.-O. (2000), Water waves over a muddy bed: A two-layer Stokes' boundary layer model, *Coastal Eng.*, **40**, 221–242.
- Ogston, A. S., D. A. Cacchione, R. W. Sternberg, and G. C. Kineke (2000), Observations of storm and river flood-driven sediment transport on the northern California continental shelf, *Cont. Shelf Res.*, **20**(16), 2141–2162, doi:10.1016/S0278-4343(00)00065-0.
- Partheniades, N. (1965), Erosion and deposition of cohesive soils, *J. Hydraul. Div. Am. Soc. Civ. Eng.*, **91**, 105–139.
- Richardson, J. F., and W. N. Zaki (1954), Sedimentation and fluidization, part 1, *Trans. Inst. Chem.*, **32**, 35–53.
- Rodi, W. (1987), Examples of calculation methods for flow and mixing in stratified flows, *J. Geophys. Res.*, **92**(C9), 5305–5328.
- Rodi, W. (1993), *Turbulence Models and Their Application in Hydraulics—A State-of-the-Art Review*, Int. Assoc. for Hydraul. Res., Delft, Netherlands.
- Rogers, W. E., and K. T. Holland (2009), A study of dissipation of wind-waves by mud at Cassino Beach, Brazil: Prediction and inversion, *Cont. Shelf Res.*, **29**, 676–690.
- Ross, M. A., and A. J. Mehta (1989), On the mechanics of luctoclines and fluid mud, *J. Coast. Res.*, **5**, 51–61.
- Sanford, L. P., and J. P.-Y. Maa (2001), A unified erosion formulation for fine sediments, *Mar. Geol.*, **179**, 9–23.
- Sheremet, A., and G. W. Stone (2003), Observations of nearshore wave dissipation over muddy seabeds, *J. Geophys. Res.*, **108**(C11), 3357, doi:10.1029/2003JC001885.
- Sheremet, A., A. J. Mehta, and J. M. Kaihatu (2005), Wave-sediment interaction on a muddy shelf, paper presented at 5th International Conference on Ocean Wave Measurements and Analysis, Am. Soc. of Civ. Eng., Madrid, Spain.
- Toorman, E. A. (1997), Modelling the thixotropic behaviour of dense cohesive sediment suspension, *Rheol. Acta*, **36**(1), 56–65.
- Toorman, E. A. (1999), Sedimentation and self-weight consolidation: Constitutive equations and numerical modelling, *Geotechnique*, **49**(6), 709–726.
- Toorman, E. A. (2008), Vertical mixing in the fully-developed turbulent layer of sediment-laden open-channel flow, *J. Hydraul. Eng.*, **134**(9), 1225–1235.
- Torres-Freyermuth, A., J. L. Lara, and I. J. Losada (2010), Numerical modeling of short- and long- wave transformation on a barred beach, *Coastal Eng.*, **57**, 317–330.
- Traykovski, P., W. R. Geyer, J. D. Irish, and J. F. Lynch (2000), The role of wave-induced density-driven fluid mud flows for cross-shelf transport on the Ealf continental shelf, *Cont. Shelf Res.*, **20**, 2113–2140.
- Traykovski, P., P. L. Wiberg, and W. R. Geyer (2007), Observations and modeling of wave-supported sediment gravity flows on the Po prodelta and comparison to prior observations from the Ealf shelf, *Cont. Shelf Res.*, **27**, 375–399.
- Trowbridge, J., and O. S. Madsen (1984), Turbulent wave boundary layers: 1. Model formulation and first-order solution, *J. Geophys. Res.*, **89**(C5), 7989–7997.
- Umlauf, L., and H. Burchard (2005), Second-order turbulence closure models for geophysical boundary layers. A review of recent work, *Cont. Shelf Res.*, **25**, 795–827.
- van Dongeren, A. R. (1997), Numerical modeling of quasi-3D nearshore hydrodynamics, *Tech. Rep. Res. Rep. CACR-97-04*, Cent. for Appl. Coastal Res., Univ. of Del., Newark, Del.
- Vinzon, S. B., and A. J. Mehta (1998), Mechanism for formation of luctocline by waves, *J. Waterw. Port Coastal Ocean Eng.*, **124**(3), 147–149.
- Wells, J. T., and J. M. Coleman (1981), Physical processes and fine-grained sediment dynamics, coast fo Surinam, South America, *J. Sed. Petrol.*, **51**, 1053–1068.
- Winterwerp, J. C. (1998), A simple model for turbulence induced flocculation of cohesive sediments, *J. Hydraul. Res.*, **36**(3), 309–326.
- Winterwerp, J. C. (2001), Stratification effects by cohesive and noncohesive sediment, *J. Geophys. Res.*, **106**(C10), 22,559–22,574.
- Winterwerp, J. C., and W. G. M. van Kesteren (2004), *Introduction to the Physics of Cohesive Sediment in Marine Environment*, Elsevier, New York.
- Winterwerp, J. C., A. J. Manning, C. Martens, T. de Mulder, and J. Vanlede (2006), A heuristic formula for turbulence-induced flocculation of cohesive sediment, *Estuarine Coastal Shelf Sci.*, **68**, 195–207.
- Winterwerp, J. C., R. F. de Graaff, and A. P. Luijendijk (2007), Modelling of wave damping at Guyana mud coast, *Coastal Eng.*, **54**, 249–261.
- Yamamoto, T., H. L. Koning, H. Sellmeijer, and E. V. Hijum (1995), On the response of a poro-elastic bed to water waves, *J. Fluid Mech.*, **87**(1), 193–206.

A. Torres-Freyermuth, Laboratorio de Ingeniería y Procesos Costeros, Instituto de Ingeniería, Universidad Nacional Autónoma de México, Sisal, Yucatan 97355, Mexico. (atorresf@ii.unam.mx)

T.-J. Hsu, Ocean Engineering Laboratory, Center for Applied Coastal Research, Department of Civil and Environmental Engineering, University of Delaware, Newark, DE 19716, USA. (thsu@udel.edu)